

JGR Solid Earth

RESEARCH ARTICLE

10.1029/2022JB026272

Key Points:

- Upper plate deformation scales with variable subducting relief, as observed along the Java Trench in seismic sections and bathymetry
- Subduction of seafloor topography induces progression from an accretion-dominated domain toward a phase of subduction erosion
- The overall low rigidity of the upper plate's base may contribute to the Java margin earthquake's tsunami-genesis

Supporting Information:

Supporting Information may be found in the online version of this article.

Correspondence to:

Y. Xia and B. Ma,
yueyangxia@hotmail.com;
yxia@geomar.de;
bma@geomar.de

Citation:

Xia, Y., Kopp, H., Klaeschen, D., Geersen, J., Ma, B., & Schnabel, M. (2023). Seamount and ridge subduction at the Java margin, Indonesia: Effects on structural geology and seismogenesis. *Journal of Geophysical Research: Solid Earth*, 128, e2022JB026272. <https://doi.org/10.1029/2022JB026272>

Received 15 DEC 2022

Accepted 5 SEP 2023

Corrected 3 OCT 2023

This article was corrected on 3 OCT 2023. See the end of the full text for details.

Author Contributions:

Conceptualization: Yueyang Xia, Heidrun Kopp, Dirk Klaeschen, Jacob Geersen

Data curation: Yueyang Xia, Heidrun Kopp, Dirk Klaeschen, Michael Schnabel

Formal analysis: Yueyang Xia, Heidrun Kopp, Dirk Klaeschen, Jacob Geersen, Bo Ma, Michael Schnabel

© 2023. The Authors.

This is an open access article under the terms of the [Creative Commons Attribution License](#), which permits use, distribution and reproduction in any medium, provided the original work is properly cited.

Seamount and Ridge Subduction at the Java Margin, Indonesia: Effects on Structural Geology and Seismogenesis

Yueyang Xia^{1,2} , Heidrun Kopp^{1,3} , Dirk Klaeschen¹ , Jacob Geersen³ , Bo Ma^{1,4} , and Michael Schnabel⁵ 

¹GEOMAR Helmholtz Centre for Ocean Research Kiel, Kiel, Germany, ²Now at Institute of Geophysics, China Earthquake Administration, Beijing, China, ³Christian-Albrechts-Universität zu Kiel, Kiel, Germany, ⁴Now at State Key Laboratory of Marine Geology, Tongji University, Shanghai, China, ⁵Bundesanstalt für Geowissenschaften und Rohstoffe (BGR), Hannover, Germany

Abstract The Java - Lesser Sunda margin, which features multi-scale subducting oceanic basement relief, is classified as neutral (Lombok and Sumbawa) to erosional (Central Java to Bali) in comparison to its accretionary counterpart offshore Sumatra. However, a comprehensive analysis of how plate boundary and upper plate structure across the neutral to erosional transition are modulated by the subduction of oceanic basement relief is lacking to date. To shed light on the tectonic parameters that push the margin into the neutral or erosional domain, we combine multi-channel reflection seismic images derived through a grid-based P-wave velocity inversion, and multibeam bathymetric maps. The data document how different scales of subducting topography modify seafloor morphology, upper plate structure, and décollement position. Large-scale subducting features cause a landward shift of the deformation front, shortening of the accretionary wedge, and seafloor steepening at the relief's trailing edge. Small-scale subducting ridges primarily impact the frontal prism resulting in over-steepening at the trench and localized slope failure. Ahead of subducting relief, deformation of the accretionary wedge encompasses enhanced compression and a reduction in seafloor slope but appears independent of the size of the relief. Ridge and seamount subduction induce frontal erosion and basal erosion offshore Lombok and Bali, respectively. Our P-wave velocity models indicate that the rigidity of the upper plate's base along the eastern Sunda margin is significantly lower than the worldwide trend. We conclude that this favors the genesis of tsunami earthquakes that have occurred on the Java margin.

Plain Language Summary The convergence of the tectonic plates drives a wide variety of geological processes along the plate margins, including the formation of the forearc accretionary wedge, volcanic activities, and megathrust earthquakes. Over the past 40 years, marine research shows that different sizes of oceanic reliefs (seamounts and ridges) are widely distributed over the seafloor, approaching the trench, and eventually subducted underneath the overriding plate. An accurate observation of the subducted reliefs and their tectonic impact on the overriding plate depends on different observation approaches, data processing methods, and the evolutionary history of the forearc. In the Java margin, the oceanic seafloor features massive seamounts with different scales and shapes, and the bathymetry of the overriding plate is highly disturbed. This provides us with the best opportunity of studying the rugged seafloor's seismogenic and geological impacts. By using state-of-the-art seismic imaging techniques, we image the subsurface structures, obtain the forearc velocity, identify the seamounts, and discuss the seamounts' effect on structural deformation and megathrust earthquake occurrence. Distinctively, the marine forearc gets shortened and thickened significantly by seamount subduction. Structural images sharply illustrate different deformation patterns and stress regimes at the seamount's different flanks and reveal the possible process of subduction erosion.

1. Introduction

Subduction of seafloor relief is widely observed at subduction zones around the globe. Different scales of subducting seamounts, basement ridges, fault scarps, or horst-and-grabens have been shown to modulate the structure and morphology of the plate interface (Bangs et al., 2006; Barker et al., 2018; Bell et al., 2010; Bonnet et al., 2019; Kodaira et al., 2000; Morton et al., 2018; Ranero & Von Huene, 2000; Tan et al., 2022), modify regional mass transport (Dominguez et al., 1998; Ruh et al., 2016; Sun, Ellis, & Saffer, 2020), and result in pervasive and potentially permanent deformation of the upper plate (Davidson et al., 2020; Martínez-Loriente et al., 2019; Todd et al., 2018; Wang & Bilek, 2011). Subducting basement relief can further modify the stress

Funding acquisition: Yueyang Xia, Heidrun Kopp
Investigation: Heidrun Kopp, Dirk Klaeschen, Jacob Geersen
Methodology: Yueyang Xia, Heidrun Kopp, Dirk Klaeschen, Bo Ma
Project Administration: Heidrun Kopp, Michael Schnabel
Resources: Heidrun Kopp, Dirk Klaeschen, Michael Schnabel
Software: Yueyang Xia, Dirk Klaeschen, Bo Ma
Supervision: Heidrun Kopp, Dirk Klaeschen
Validation: Yueyang Xia, Heidrun Kopp, Dirk Klaeschen
Visualization: Yueyang Xia, Dirk Klaeschen
Writing – original draft: Yueyang Xia, Heidrun Kopp
Writing – review & editing: Yueyang Xia, Heidrun Kopp, Dirk Klaeschen, Jacob Geersen, Bo Ma, Michael Schnabel

distribution (Lallemand & Le Pichon, 1987; Ruh, 2016; Ruh et al., 2016) or enhance fluid expulsion into the subduction zone (Chesley et al., 2021; Sun, Saffer, & Ellis, 2020; von Huene et al., 2004).

Oceanic basement features vary in height, composition, and surface morphology and exhibit a wide variety of forms, comprising conical shapes (peaked or flat-top), multiple branches, or parallel ridges (Figures 1b and 1c). Seamounts, which represent one of the most common and most widespread topographic features on oceanic plates, have been documented within numerous subduction zone systems, including Tonga-Kermadec (Timm et al., 2013), Nankai (Bangs et al., 2006), Japan and Kuril (Lallemand et al., 1989), Cascadia (Tréhu et al., 2012), Hikurangi (Bell et al., 2014), northern Chile (Ma et al., 2023), and Central America (Ranero & Von Huene, 2000). Upper plate deformation associated with seamount subduction is manifested by re-entrants or scarps at the margin toe (Ranero & Von Huene, 2000), gravitational submarine landslides (Brune et al., 2010), strike-slip faulting (Davidson et al., 2020), regional uplift (Laursen et al., 2002) or the landward shift of the deformation front (Kopp et al., 2006). Underthrusting of basement topography can induce localized uplift and gravitational collapse of the forearc (e.g., Hühnerbach et al., 2005; Kopp et al., 2006; Ruh, 2016). Furthermore, underthrusting topography is a driving factor of subduction erosion, which removes material from the toe of the overriding plate as well as from its base. Structural erosive packages removed from the upper plate related to seamount or oceanic relief subduction are documented in seismic studies (Edwards et al., 2018; Marcaillou et al., 2016).

Subduction of seafloor topography has been associated with marine geohazards including submarine landslides, earthquakes, and related tsunamis. A long-standing, controversial discussion has focused on the relationship between the subducted seamount and the generation of large earthquakes. This is based on the intuitive hypothesis that the positive relief would increase normal stress along the plate interface, resulting in enhanced coupling patches, which would favor large earthquakes (Cloos, 1992; Cloos & Shreve, 1996; Scholz & Small, 1997). The Java 1994 tsunami earthquake ($M_w = 7.8$) has been discussed as a slip over a subducted seamount (Abercrombie et al., 2001; Bilek & Engdahl, 2007), though the seamount's exact location remains ambiguous due to sparse data coverage (Xia et al., 2021). Recent discussions (Wang & Bilek, 2014) and modeling results (Ruh et al., 2016; van Rijnsingen et al., 2019; Yang et al., 2013), however, imply that seamounts or bathymetric basement highs favor aseismic creeping or smaller magnitude earthquakes ($M_w < 7$), and potentially act as seismic barriers due to complex faulting and heterogeneous stresses in their vicinity.

Here we discuss the impact of oceanic basement relief at various scales, ranging from seamounts to ridges to smaller-scale relief such as subducting fault scarps. Our analysis is based on four re-processed and depth-migrated multi-channel seismic (MCS) profiles from the Java-Lesser Sunda forearc. The grid-based tomography and pre-stack depth migration (PSDM) provide seismic images with corrected reflector dipping angles. The seismic images reveal the scale-dependent effect of the subducting topography on the geometry and deformation of the marine forearc and the accretionary wedge as well as on the evolution of the décollement. Our study documents how the scale of subducting relief modifies the pattern, areal extent, and magnitude of plate interface and upper plate deformation across the neutral (Lombok and Sumbawa) to erosional (Central Java to Bali) Java-Lesser Sunda margin.

2. Tectonic Setting of the Java-Lesser Sunda Margin

The ~5,000 km long Sunda arc extends westward from Flores to Java and then trends northwest toward Sumatra and Myanmar (Hamilton, 1988) (Figure 1). The tectonic evolution of the Sunda arc is driven by the subduction of the Indo-Australian plate underneath Eurasia since the Eocene-Oligocene (Hall, 2002; Hall & Smyth, 2008; Hamilton, 1988; Moore et al., 1982), following the Eocene collision of India with Eurasia. Given its great lateral extent, tectonic parameters vary along the Sunda forearc (McNeill & Henstock, 2014; Moore et al., 1980). The oceanic lithosphere's age decreases toward the west from 150 Ma offshore Sumba to 125 Ma off Bali, reaching 90 Ma off Sumatra (Heine et al., 2004). Offshore Java and the Lesser Sunda Islands, the subduction orientation is almost orthogonal with a convergence rate of 67 mm/yr in a direction $N 11^\circ E \pm 4^\circ$ (Bock et al., 2003; Tregoning et al., 1994) (Figure 1). Information on the crustal structure of the Java-Lesser Sunda marine forearc is mostly based on the analysis of a suite of wide-angle and MCS seismic lines (Karig et al., 1980; Kopp et al., 2006, 2009; Lüschen et al., 2011; Moore et al., 1980; Müller et al., 2008; Planert et al., 2010; Shulgin et al., 2011). An overview of the main geological parameters for each seismic profile presented here is provided in Table 1.

Offshore central Java around $109^\circ E$, the tectonic regime changes from subduction accretion to subduction erosion. This change is related to the underthrusting of the Roo Rise oceanic plateau, which composes the eastern portion of the Christmas Island seamount province, off central and eastern Java ($109^\circ E$ to $115^\circ E$) (Kopp et al., 2006)

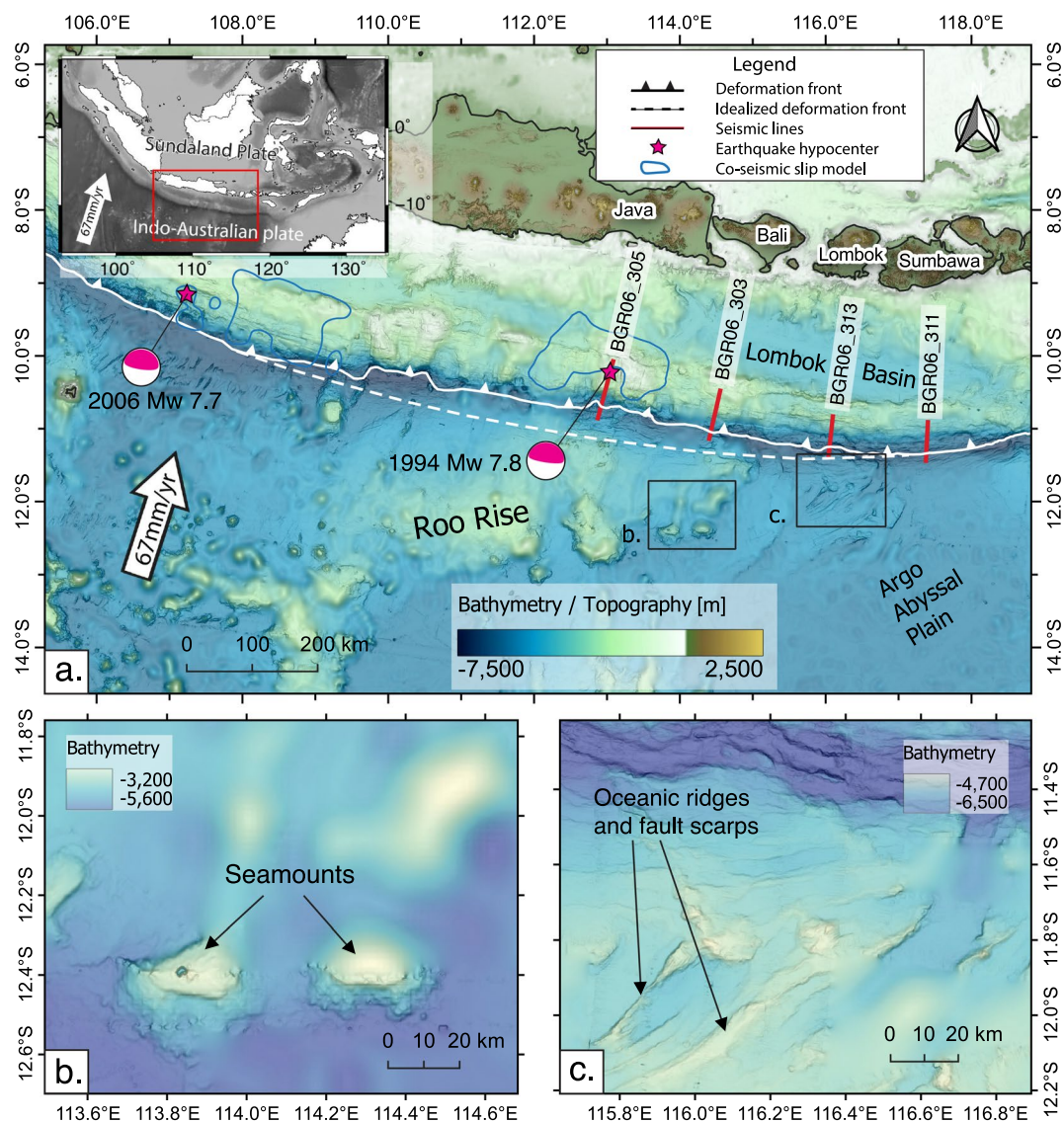


Figure 1. (a). Regional tectonic setting and bathymetry of the study area. Red lines indicate the location of the four MCS profiles. The deformation front is traced by the solid white line, and the undisturbed hypothetical trend of the deformation front is shown by the white dashed line. Stars indicate the 1994 Mw 7.8 and 2006 Mw 7.7 earthquake hypocenters, and the blue solid lines show the coseismic slip of the earthquakes (Bilek & Engdahl, 2007). Earthquake focal mechanisms are derived from the global CMT project. (b) A close-up view of the conical seamounts observed on the oceanic crust of the Roo Rise. (c) A close-up view of the linear-shaped ridges on the oceanic crust offshore Lombok.

Table 1
Measured Geometrical Parameters of the Marine Forearc in Different Seismic Sections

MCS line number	The surface slope of the mature accretionary wedge/middle slope [°]	Water depth [km] at the trench	Water depth [km] of slope break	Water depth [km] of forearc high	Distance between the deformation front and the slope break [km]	Distance of the trench retreat [km]	Length of the accretionary wedge [km]
BGR06_311 (Sumbawa)	5.0	6.65	3.62	2.80	43	0	68
BGR06_313 (Lombok)	—	6.62	2.75	2.38	43	16	77
BGR06_303 (Bali)	7.6	5.92	2.27	1.52	37	30	82
BGR06_305 (Eastern Java)	8.3	6.30	2.34	0.75	32	50	99

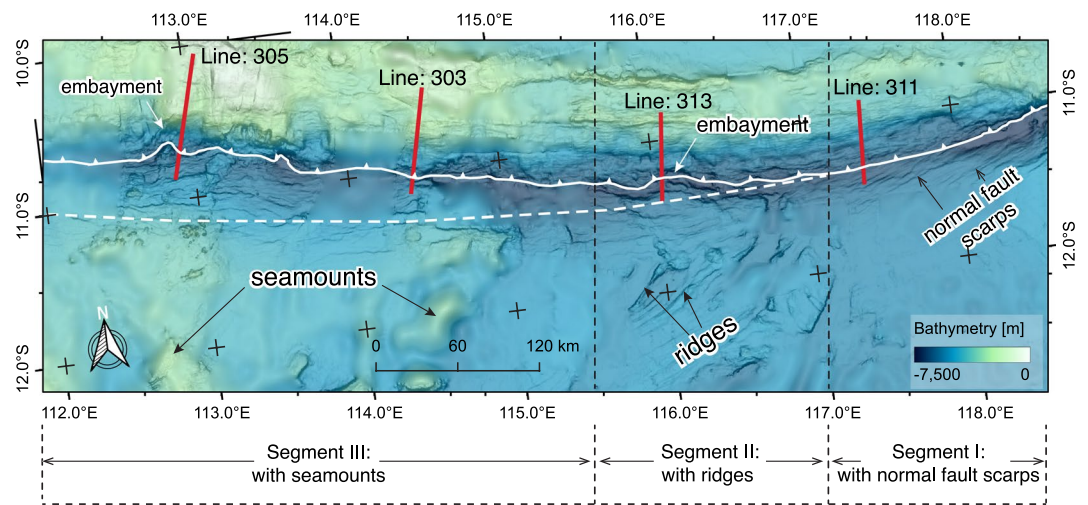


Figure 2. Bathymetry map around profiles BGR06_313 (off Lombok), BGR06_311 (off Sumbawa), BGR06_303 (off Bali), and BGR06_305 (off eastern Java). The solid white line indicates the deformation front, and the white dashed line illustrates the idealized trend of the deformation front. Please note that the study area could be divided into three different geological units (segments) along the strike. In Segment I from $\sim 117^{\circ}\text{E}$ to $\sim 118.5^{\circ}\text{E}$, the oceanic plate is devoid of a large seamount or basement ridge, but features minor bending-related normal faults with a small offset (<150 m) close to the trench. The oceanic plate in Segment II from $\sim 115.5^{\circ}\text{E}$ to $\sim 117^{\circ}\text{E}$ carries linear-shaped ridges on the oceanic crust. Segment III from $\sim 112^{\circ}\text{E}$ to $\sim 115.5^{\circ}\text{E}$ is characterized by numerous conical or semi-conical shape seamounts on the oceanic plate.

(Figure 1). In the projection of the Roo Rise from central Java to Bali, subduction erosion causes a deflection of the Java trench and outer forearc toward the arc by ~ 40 km from the idealized curvature trend of the deep-sea trench (Krabbenhoef et al., 2010). The Roo Rise is manifested in a ~ 500 km broad plateau that extends over $100,000$ km² offshore central and eastern Java (Shulgin et al., 2011). It is dotted with isolated seamounts with an average elevation of $>2,000$ m above the surrounding ocean floor (Figure 1b). The formation of the Christmas Island seamount province is linked to the shallow recycling of the continental lithosphere entrained in the mantle (Hoernle et al., 2011). Refraction tomography studies have shown that the Roo Rise crustal thickness close to the trench is between 12 and 18 km, with a relatively low P-wave velocity for conventional oceanic crust (Shulgin et al., 2011) ($v_p = 6.6$ km/s compared to $v_p = 7.2$ km/s at the oceanic Moho). The marine forearc morphology offshore eastern Java is significantly modulated by the distinct lower plate topography of the Roo Rise entering the trench. Local landslide scarps, frontal embayments (concave-shaped 'cookie bites' or re-entrants), and over-steepened surface slopes, which are interpreted as evidence for mass failure, are observed at the lower slope (Kopp, 2011) (Figure 1a, e.g., at 110°E , 112°E , 113°E).

The easternmost segment of the Sunda forearc is characterized by the underthrusting of the Argo abyssal plain offshore Lombok and Sumbawa islands (115°E to 119°E) (Figure 1). With a mean water depth of 5,500 m, the Argo abyssal plain is largely devoid of terrigenous sediment (Moore et al., 1982; Planert et al., 2010). The crust of the Argo abyssal plain has a thickness of ~ 8.6 km, indicating a very mature oceanic crust of ~ 128 Ma to 150 Ma (Seton et al., 2020). The morphology of the seafloor turns from rugged offshore Bali to generally smooth offshore Sumbawa (Lüschen et al., 2011) (Figures 1 and 2). Offshore Lombok (at $\sim 116^{\circ}\text{E}$), linear-shaped oceanic basement structures trending NE-SW (45° – 60°) roughly parallel to the magnetic anomalies characterize the seafloor (Figure 2 & Figure S1 in Supporting Information S1) (Lüschen et al., 2011). On the outer trench slope landward of the outer rise, an extensive pattern of plate-bending induced normal faults with throws up to 150 m and individual fault segment lengths of up to 60 km is observed starting at about 30 km seaward of the trench axis (Figure 2) (Lüschen et al., 2011). The bathymetry and MCS data show a strong horst-and-graben relief in the trench, which is the surface expression of bend faults that have been imaged to cut deep into the oceanic basement (Lüschen et al., 2011).

To the north, the mature Lombok forearc basin (Figure 1a) has an average water depth of 4,400 m and is bound by the Roo Rise subduction to the west and the Scott plateau to the east (Planert et al., 2010) (Figure 1). The basin and the adjacent forearc high are uniformly developed along the entire Lombok segment and remain largely undisturbed by the subduction of the pronounced basement relief. This stands in contrast to the Roo Rise segment

off eastern Java and Bali further west, where the forearc high rises to a water depth of less than $\sim 1,500$ m compared to $\sim 2,300$ – $3,000$ m offshore Lombok-Sumbawa (Krabbenhoeft et al., 2010).

3. Data and Methods

The MCS reflection data used in this study were collected by the Federal Institute for Geosciences and Natural Resources (BGR) (Müller & Neben, 2006) on RV SONNE cruise SO190 during the SINDBAD Project in 2006. We analyzed four trench-dipping MCS profiles (BGR06_311, BGR06_313, BGR06_303, and BGR06_305), which cover the marine forearc offshore Sumbawa, Lombok, Bali, and eastern Java, respectively (Lüschen et al., 2011; Planert et al., 2010; Shulgin et al., 2011) (Figures 1 and 2; Table 1). The seismic source used in the survey is a G-Gun array. The source was towed at a water depth of 6 m and has a maximum total volume of $3,100 \text{ in}^3$ (50.8 l). Seismic signals were recorded by a 240-channel digital streamer with a length of 3,000 m.

Previous processing of the seismic data was based on a work flow including common mid-point (CMP) binning, multiple attenuation with Radon filter and wave equation-based prediction, velocity analysis using the focusing technique, and Kirchhoff PSDM (Lüschen et al., 2011). In the new processing routine of this study, the major difference is how the PSDM images are iteratively updated in the Kirchhoff PSDM. We used the ray-based reflection tomography method with the Non-Rigid Matching (NRM) depth warping technique (Xia et al., 2022) to refine the vp model at shallow depth (< 3 km below seafloor) and to improve imaging of the shallow sediment structure.

Seismic profiles BGR06_303, BGR06_305, BGR06_311, and BGR06_313 are processed using a work-flow that includes geometry set-up, common midpoint (CMP) binning (binning size of 6.25 m, CMP fold of 30), zero-offset traces padding, bandpass filtering, shot interpolation (2 times), and random noise attenuation (Xia et al., 2021). The strong multiple reflection caused by the shallow water depth of the forearc high is suppressed by a free surface-related multiple prediction based on the Kirchhoff integral (Verschuur et al., 1992). By using adaptive subtraction (Guitton & Verschuur, 2004), the multiple was eliminated with a cascaded frequency band (Xia et al., 2021). The initial interactive semblance velocity analysis of these four profiles is calculated in the time domain with an analyzed CMP distance of 250 m and converted to the depth domain. The vp models are subsequently merged with the ocean bottom seismometer (OBS) refraction models of Shulgin et al. (2011) and Planert et al. (2010), except for profile BGR06_303 and BGR06_311, for which no coincident OBS profiles exist. A smooth taper zone at the base of the MCS-derived model was used while merging the refraction vp models to avoid any abrupt changes in the vp models. The PSDM with the vp model establishment was performed in the depth domain and iteratively refined the vp model and MCS PSDM image by using the ray-based reflection tomography with a warping technique to minimize the residual depth move-out (Xia et al., 2022). The deconvolution is applied within the step of the Kirchhoff depth migration, in order to simplify and sharpen the source signature. One example of the improvement of the seismic imaging compared to the study of Lüschen et al. (2011) is the subsurface structure of the MCS profile BGR06_311. The previous interpretation identified a large thrust fault in the oceanic plate based on the undulation of the plate interface reflection (Figure 8 in Lüschen et al., 2011). Migration and velocity inversion reveal that this structural undulation imaged in Lüschen et al. (2011) resulted from an inappropriate uniform upper plate velocity (Figure S2 in Supporting Information S1). The re-processed seismic image reveals that the oceanic plate and the décollement below the accretionary wedge are affected by bending-related normal faults in the subsurface (Figure 3a), rather than thrust faulting.

The multibeam bathymetric data in this study were collected during the RV. SONNE SO190 cruise (Kopp, 2011), using a 12 kHz SIMRAD EM120 multibeam device with a 90° opening angle resulting in a swath width of 2 times the water depth. A sea water velocity profile was collected at the beginning of the cruise. Subsequent processing was performed by using the MB System software (Caress & Chayes, 1996). The quality of the data was good to excellent in spite of several days of high waves producing some bad signals and typical problems with the bottom detect algorithm on steep flanks facing away from the ship. The processed data were gridded with the Generic Mapping Tools (GMT) software (Wessel & Smith, 1991) using a near-neighbor gridding algorithm and subsequently imported into QGIS. Regions not covered by the multibeam survey were filled with the GEBCO_2020 bathymetry (GEBCO, 2020).

4. Results

We present the four 2-dimensional (2D) MCS profiles and P-wave velocity structures (Figures S3–8 in Supporting Information S1) covering the trench and lower slope of the Eastern Java-Lesser Sunda margin starting with the easternmost profile offshore Sumbawa and progressively moving westwards toward Java (Figure 1, Table 1). Generally, 2D MCS images in a complex 3D topography suffer from contamination by out-of-plane structures,

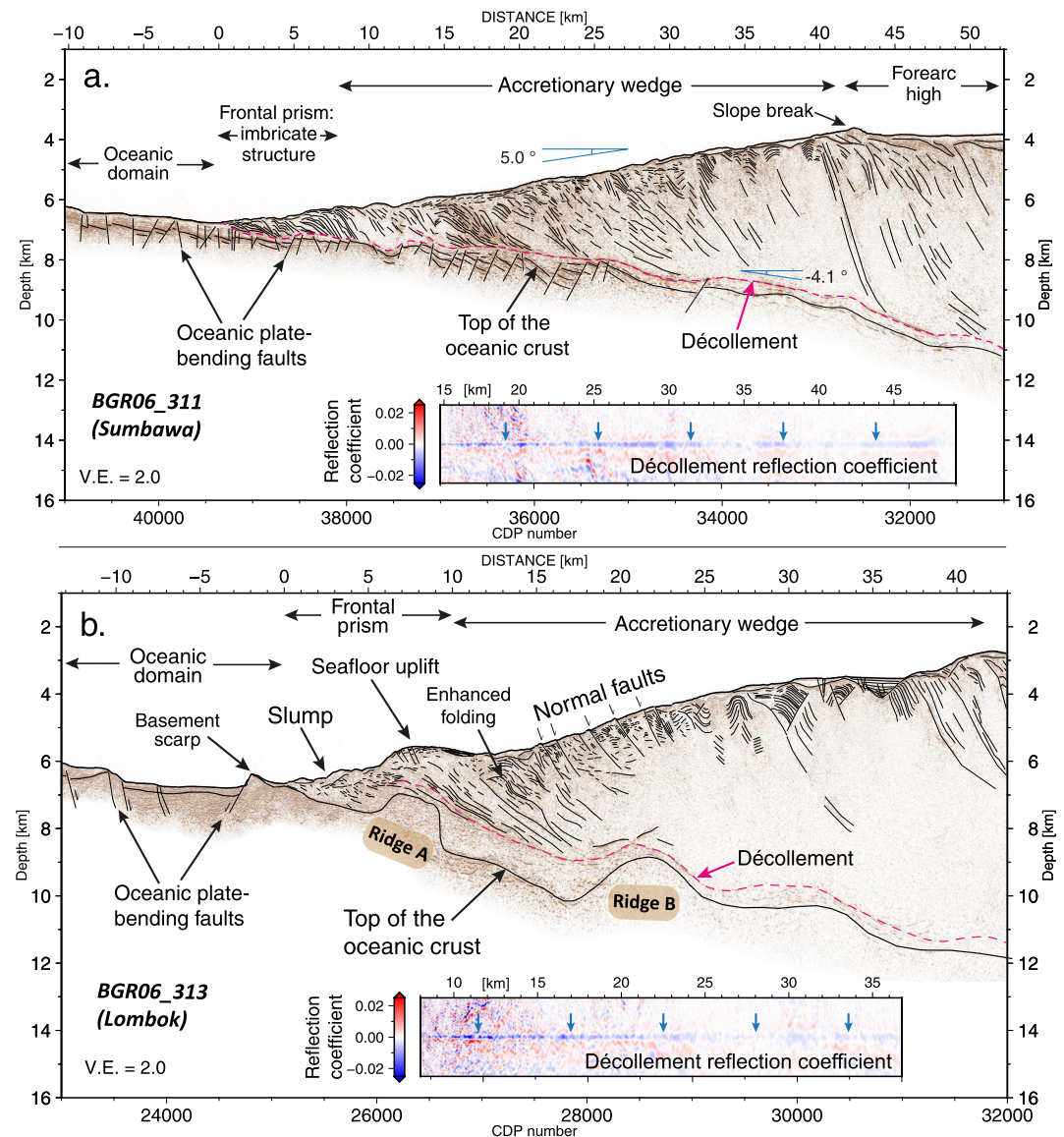


Figure 3. (a) MCS depth migration image and the line-drawing of the seismic line BGR06_311 offshore Sumbawa. (b) MCS depth migration image and the line-drawing of the seismic line BGR06_313 offshore Lombok. The reflection coefficient of the horizontally aligned décollement is plotted within each subfigure.

and the true dip and depth of the reflectors cannot be imaged as precisely as in a 3D seismic survey. Please note that such shortcomings are unavoidable no matter how sophisticated the processing methods are.

The easternmost profile BGR06_311 offshore Sumbawa serves as a reference line for the plate boundary and upper plate accretionary wedge structure, which along this profile is not significantly affected by large-scale (>150 m) subducting relief (Figures 2 and 3a). Profiles BGR06_313 (offshore Lombok), BGR06_303 (offshore Bali), and BGR06_305 (offshore eastern Java), in contrast, are characterized by the subduction of oceanic basement relief of various dimensions, including basement ridges and seamounts. An overview of the different features is provided in Table 2. In the following presentation of the seismic profiles, we distinguish between the oceanic domain (outer rise and trench), the active frontal prism, the mature accretionary wedge, and the forearc high as the main tectonic units.

4.1. Profile BGR06_311—Offshore Sumbawa

MCS profile BGR06_311 is located offshore Sumbawa where the Argo Abyssal plain is subducting below the island arc (Figure 1). The incoming oceanic crust carries about 420 m of sediment (Figure 3a, S3 in Supporting

Table 2

Approximated Physical Characteristics of the Subducting Seamounts and Ridges in Seismic Sections

Subducting relief ID	Height [km]	Width [km]	Aspect ratio	Distance to trench [km]	Depth (abs) [km]	Depth (below seafloor) [km]	Relief type	Elapsed time of the relief subduction (ka)
Ridge A in BGR06_313	1.3	4.5	0.28	7	7	1.5	Basement Ridge	150
Ridge B in BGR06_313	1.6	6.3	0.25	22	8.5	3.5	Basement Ridge	400
Ridge in BGR06_303	1.3	4.1	0.31	7	5.5	0.5	Basement Ridge	130
Seamount in BGR06_303	2.1	26.2	0.08	36	8	5	Seamount	700
Seamount in BGR06_305	2.7	39.3	0.07	33	7.5	5.5	Seamount	850

Information S1, km –10 to 0). In the trench, approximately 500–600 m of sediment has accumulated. This portion of the Java-Lesser Sunda margin (termed Segment I in Figure 2) is not significantly affected by seamount subduction or frontal subduction erosion, which induces a northward deflection of the deformation front further west (Figure 1a). The incoming seafloor is much smoother than in the Roo Rise domain (Segment III in Figure 2) to the west and no large-scale (>500 m height) topographic features are observed seaward of the trench (Figure 2). The high-resolution bathymetry data reveal bending-related normal fault scarps (vertical throw <150 m) on the outer rise (Figures 2 and 4a), aligned parallel to the magnetic isochrons (Figure S1 in Supporting Information S1) and trending obliquely to the strike of the deformation front. The faults dissect the oceanic basement and the overlying sediment cover (Figure 3a, km –10 to 0). As the plate subducts, the fault throw is enhanced due to the increased bending of the oceanic crust, resulting in a horst-and-graben structure of the oceanic basement with moderate offsets (100–500 m) underneath the frontal prism (Figure 4c) and the accretionary wedge (Figure 4b). A previously interpreted thrust

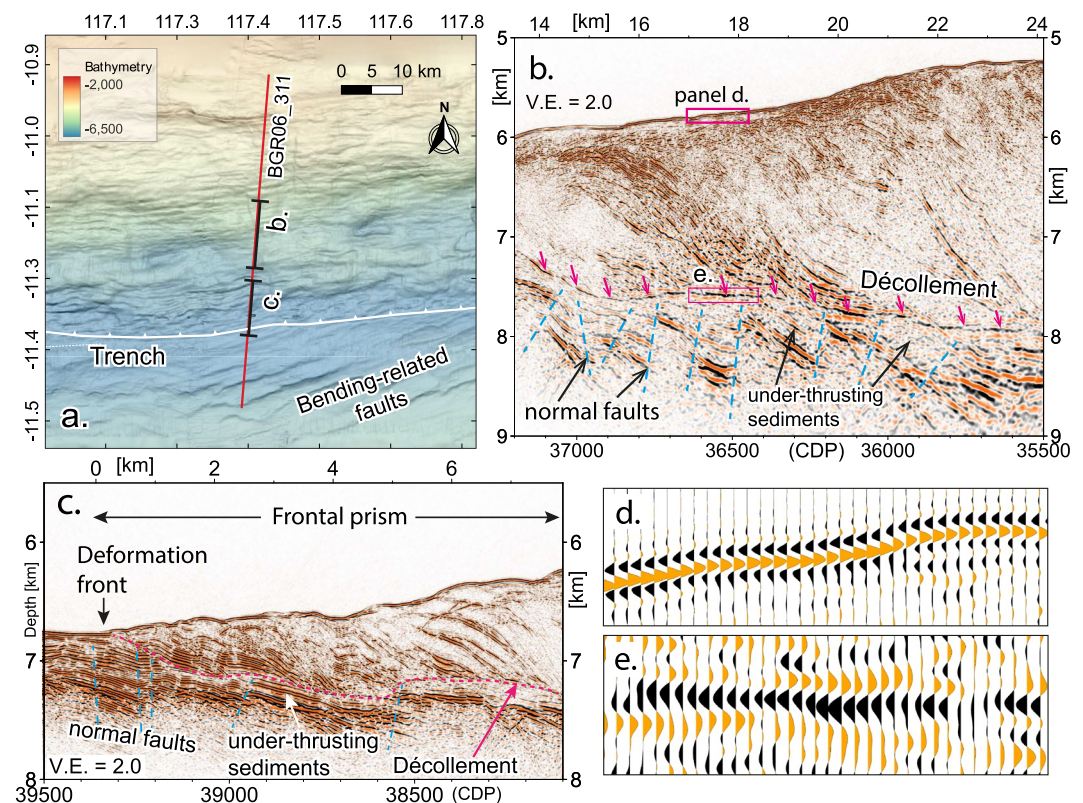


Figure 4. (a) Bathymetry map around profile BGR06_311. (b) Close-up view of the upper plate lower slope. Plate-bending induced normal faulting affects the oceanic basement. The plate interface reflection features a reversed polarity wavelet compared to the seafloor reflection (compare panels d and e). (c) Close-up view of the trench and frontal prism. (d) Zoom-in wiggle display of the seafloor reflection. (e) Zoom-in wiggle display of the décollement reflection. Orange in-fill indicates positive polarity, and black color in-fill indicates reversed polarity.

fault, dissecting the entire oceanic crust down to Moho depth (Figure 8 in Lüschen et al., 2011) is not in the new depth migrated seismic section presented here by correcting the velocity model (Figure S2 in Supporting Information S1). Landward of the deformation front (profile km 0), approximately 60% of the incoming sediment sequence is frontally accreted, while the remaining part constitutes a band of underthrust material with a thickness of ~170 m (Figure 4c). The frontal prism on this profile (km 0 to 8) is a textbook example of frontal sediment accretion and documents the formation of imbricate thrusts that progressively steepen and rotate landwards to accommodate the incoming material (Figure 4c). Approximately 8 km landward of the deformation front, the upper plate reflectivity decreases and marks the transition from the actively accreting frontal prism to the mature accretionary wedge (Figure 3a, km 8 to 41). Landward dipping fore-thrusts and imbricate sediment layers are observed in the accretionary wedge, connecting from the seafloor to the plate boundary at depth (e.g., at around profile km 13 and 20, Figure 3a). The thrust faults cause minor seafloor offsets and undulations at the lower and middle slope (e.g., around profile km 21 to 23) (Figure 3a). The surface slope of the accretionary wedge (Figure 3a, km 10–41) is relatively uniform at ~5°. A prominent slope break at profile km 42 coincides with a steeply dipping reflector that offsets the seafloor and cuts through the accretionary wedge to connect to the megathrust at 9.5 km depth (Figure 3a). The décollement is imaged as a coherent reflector from profile km 14 to 50 (Figure 3a) and is characterized by a reversed polarity relative to the seafloor's wavelet (Figures 4d and 4e). The plate interface dipping angle is around -4.1° underneath the frontal prism and accretionary wedge (Figure 3a, km 5–40).

4.2. Profile BGR06_313—Offshore Lombok

Profile BGR06_313 trends offshore Lombok, approximately 140 km west of the Sumbawa profile BGR06_311 (Figures 1 and 2). The outer rise offshore Lombok carries a number of linear-shaped ridges (Figure 1c, & Segment II in Figure 2). Here, the trench is partially devoid of any sediment and isolated sediment patches reach a thickness of less than 150 m (Figure 3b, km -10 to 0), though a sediment cover of 400–500 m is observed on the incoming crust (Lüschen et al., 2011; Planert et al., 2010). The deformation front in this region along the margin (116.1°E) starts to deviate from the normal trend of the trench (Figure 1, white stippled line), which has previously been attributed to frontal erosion caused by the subduction of pronounced sea plateau (Kopp et al., 2006). At the location where line BGR06_313 crosses the trench, a ~30 km wide embayment at the lower slope is visible in the seafloor bathymetry (Figure 2). The frontal prism, as observed on the neighboring line BGR06_311 to the east, is disrupted and features little imbricate structure (Figures 3b and 5a, profile km 0 to 10). The deformation front exact location on the profile is obscured by a steep oceanic basement scarp (around profile km -2) with a vertical throw of ~600 m which is currently entering the subduction system (Figure 3b).

On the subducting crust, a ~1.3 km height oceanic basement high (Ridge A in Figures 3b and 5a, Table 2) is found at a depth of 7 and ~1.5 km below the seafloor (Figures 3b and 5a, profile km 5 to 10) underneath the frontal prism. It coincides with a shallowing of the seafloor by about 1,000 m (Figure 5a), where a local seafloor bulge (profile km 6 to 11) extends laterally in a trench-parallel direction for ~30 km (Figure 5b, Ridge A). Landslide scars on the trenchward flank of the seafloor bulge (Figure 5b) are recognized in the bathymetry map and coincide with the chaotic and discontinuous nature of the shallow sedimentary strata in the frontal prism as described above (Figure 5a km 0 to 6). An anomalous strong reflection band (Figure 5a, at CDP 26400 to 26,700, depth 8.5–9 km) is observed below the top of the oceanic crust. This reflection band likely originates from either upper oceanic crustal reflections which have been observed in the oceanic domain (Figure S9 in Supporting Information S1) or from out-of-plane signals.

Further downdip, a second subducting basement high (Ridge B) with a height of approximately 1.6 km (Table 2) (Figures 3b and 5c, profile km 17–23) coincides with a seafloor surface slope of 9° (Figure 5c). Shallow landward dipping normal faults offsetting the seafloor (Figure 5d) are observed here. The internal reflection pattern of the accretionary wedge is characterized by complex and small-scale reflectors (Figure 5d).

The décollement, which parallels the oceanic basement reflection further downdip (Figure 3b, profile km 21 and beyond), deviates from the basement between the two basement highs (Ridges A and B) and trends more than 1 km above the top of the oceanic crust (Figure 3b, profile km 10–21), migrating upward on the leading flank of Ridge A (Figure 5a, km 6 to 10). It is characterized by a band of reflectors showing a negative reflection coefficient (Figures 3b and 5e).

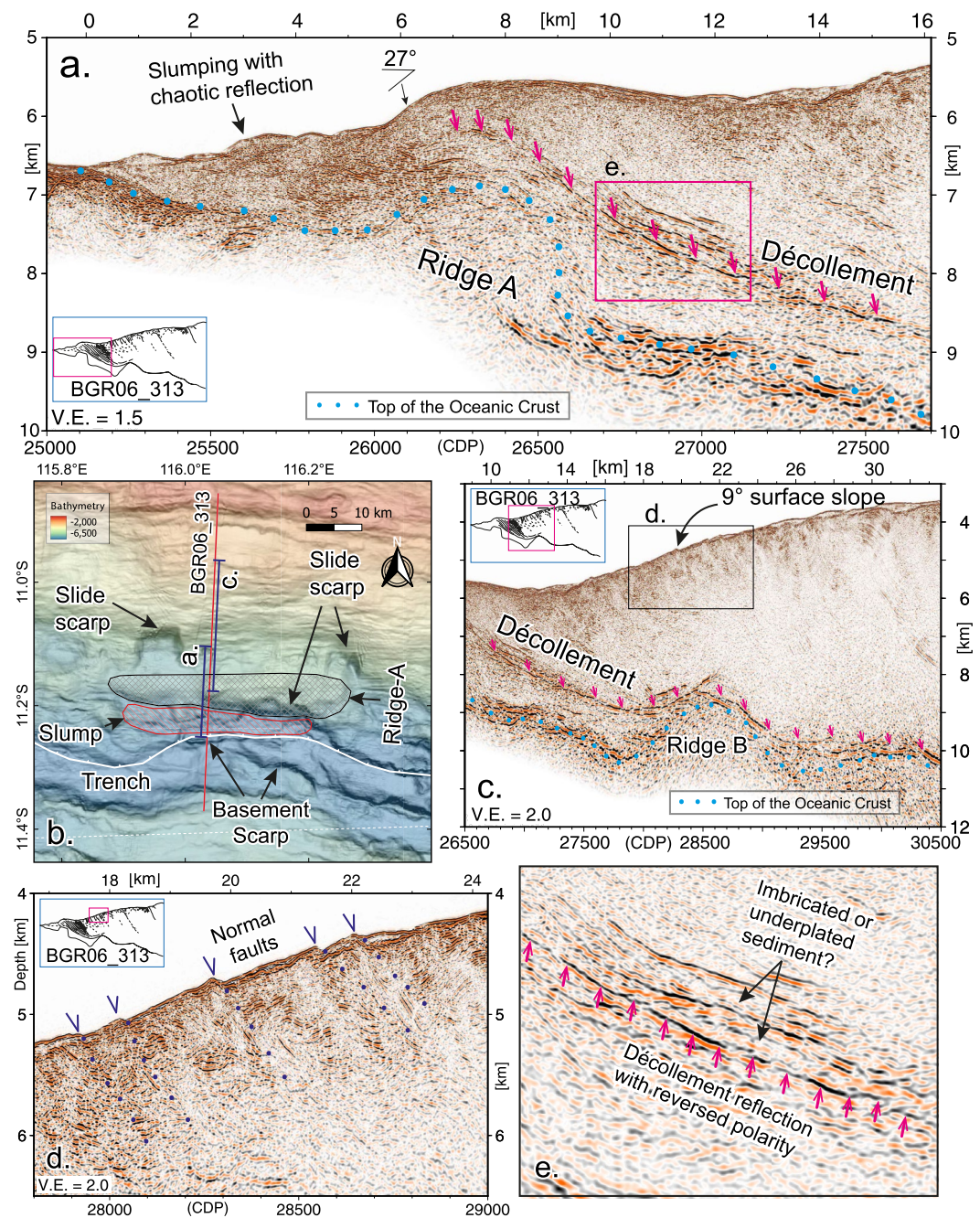


Figure 5. (a) Close-up view of subducting Ridge (a) Uplift of the upper plate causes a seafloor bulge above the subducting ridge. Mass wasting deposits seaward of Ridge A are featured by a chaotic internal reflection pattern. (b) Upper plate seafloor morphology modulated by subducting ridges offshore Lombok around profile BGR06_313. (c) Close-up view of subducting Ridge (b) Trend of the décollement indicated by red arrows. Blue dots indicate the oceanic basement. (d) Close-up view of the upper plate above Ridge (b) Please note that the normal faults (marked by dark blue dots) crop out at the seafloor, indicating recent fault activity. (e) Close-up view of the décollement between Ridge A and Ridge (b) The reversed polarity reflectors are marked by red arrows.

4.3. Profile BGR06_303—Offshore Bali

Profile BGR06_303 is located offshore Bali where the easternmost portion of the Roo Rise with its significant basement relief is currently entering the trench (Segment III in Figure 2). At profile km 6 to 11, the seafloor is uplifted by a subducting basement ridge (Figures 6a and 7c), also traced in the bathymetry as a 12 km long escarpment (Figure 7a, in the black polygon). This situation is similar to profile BGR06_313 (Figure 5a). The ridge

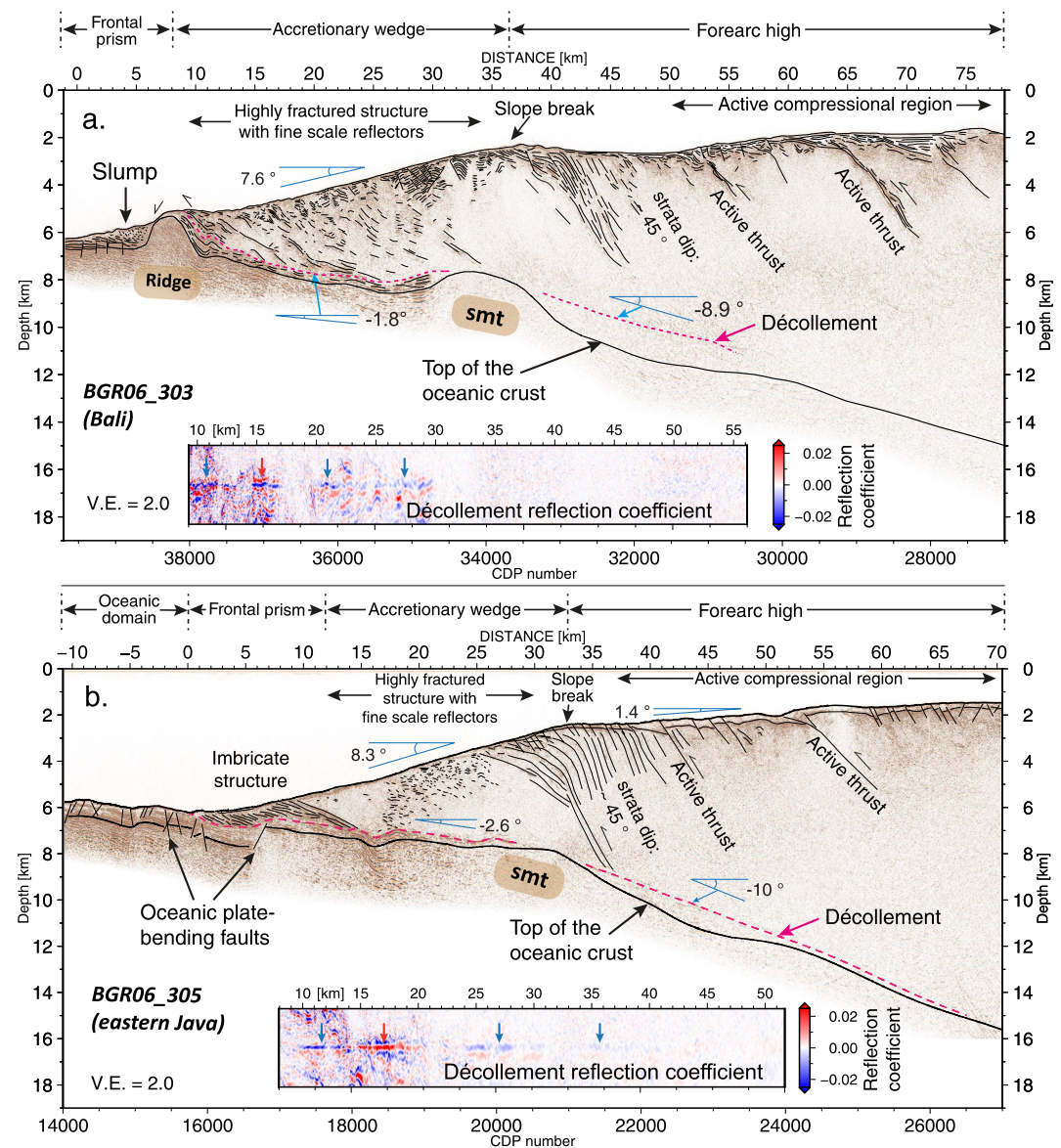


Figure 6. (a) MCS depth migration image and the line-drawing of the seismic line BGR06_303 offshore Bali. (b) MCS depth migration image and the line-drawing of the seismic line BGR06_305 offshore eastern Java. The reflection coefficient subgraph of horizontally aligned décollement is plotted within each subfigure.

disrupts the stratigraphy of the frontal prism causing significant compression as it is underthrust underneath the lowermost slope. Landward of the subducting ridge, the internal structure of the upper plate is deformed by strong folding (Figure 7c). The underthrust sediment is observed with an average thickness of 600 m (Figure 7c). At the trailing side of the subducting ridge, the oceanic sediment is covered by a chaotic reflection unit with weak amplitudes (Figures 6a and 7c, km 2 to 6). Several layers of sub-parallel reflections could be observed underneath the top of the oceanic crust (Figure 7c). We interpret these reflections as oceanic upper crustal structures which are also observed in the oceanic domain (Figure S9 in Supporting Information S1). Similar reflections in the upper oceanic crust or below seamounts are also observed in MCS surveys of other oceanic settings and subduction zones for example, Juan de Fuca, Lesser Antilles, Alaska, Costa Rica and the Pacific (Han et al., 2018; Kodaira et al., 2014; Marcaillou et al., 2021; Ranero et al., 1997). These studies have interpreted these reflections as sheeted dikes or discrete shear planes (Ranero et al., 1997). These structures would be preserved and imaged by the MCS survey when the oceanic crust is subducted underneath the toe of the upper plate at a shallow depth.

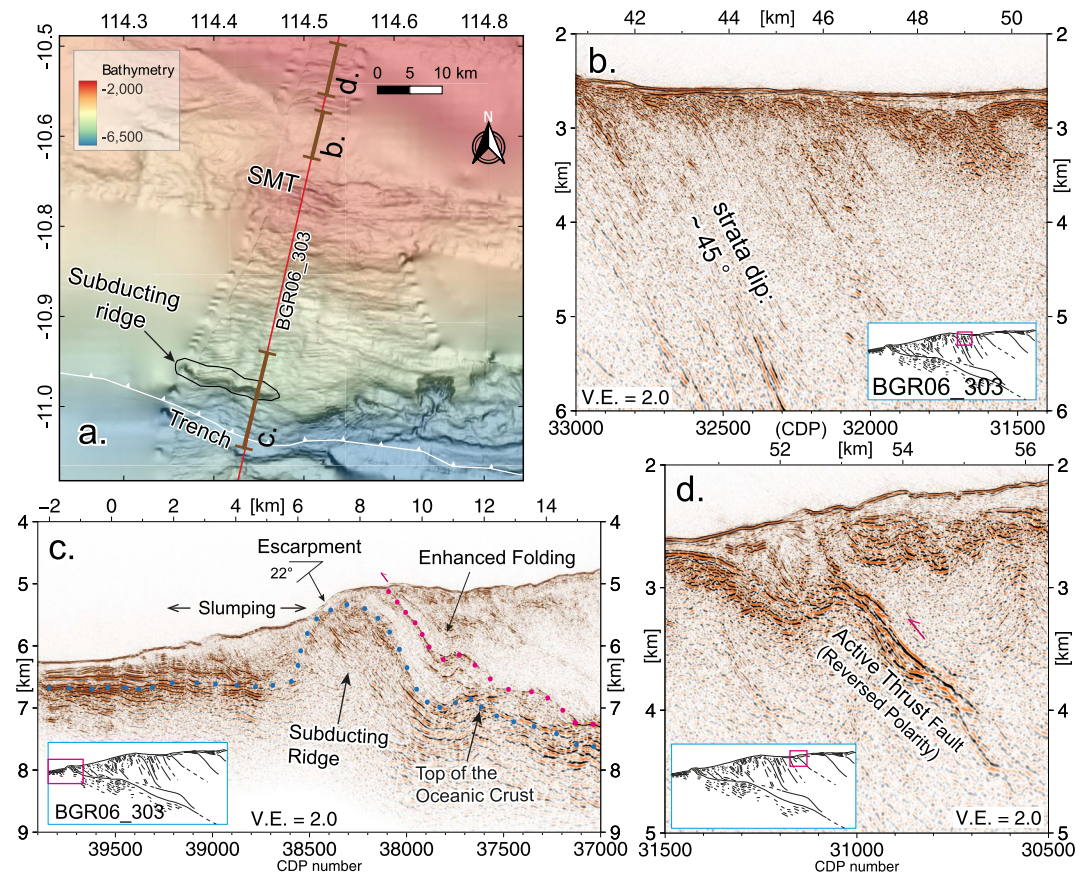


Figure 7. (a) Upper plate deformation induced by a subducting oceanic basement topography offshore Bali close to profile BGR06_303. (b) Upper plate close-up view of the $\sim 45^\circ$ dipping reflectors in front of the subducting seamount. (c) Close-up view of frontal prism and lower accretionary prism where a subducting basement ridge causes seafloor uplift resulting in a local steep slope angle of 22° . Upper plate deformation in response to the under-thrusting ridge is expressed in enhanced folding in front of the ridge. The décollement is marked by red dots. (d) Close-up view of an active thrust fault landward of the seamount. The thrust fault features a reversed polarity wavelet compared to the seafloor's reflective wavelet.

Above the accretionary wedge, the seafloor shows an average slope of 7.6° (Figure 6a, km 12 to 35) (Table 1). A seafloor slope break at profile km 36–40 corresponds to the surface outcrop of a high-amplitude landward dipping reflector. Landward of the slope break, the seafloor slope becomes shallow to horizontal between profile km 40 and 52 (Figure 6a). The shallow water depth (1,500 m) and active thrusting of the accretionary wedge forearc high (most pronounced around profile km 53 and 64), which offsets the seafloor, document the compressional state of this domain (Figure 6a, km 50–77). The thrust fault at profile km 53 to 55 is characterized by a reversed polarity (Figure 7d) compared to the seafloor reflection. The sedimentary strata from km 41 to further landward has been rotated to an angle of $\sim 45^\circ$ (Figure 7b).

Underneath the slope break between profile kilometers 30 to 45, a subducting seamount is identified at a depth of 8–10 km (Figure 6a). It coincides with a semi-conical bulge in the seafloor bathymetry (Figure 7a). Landward of the leading flank of the seamount, the décollement lies 1,200 ~ 1,800 m atop the oceanic crust (Figure 6a, S5 in Supporting Information S1, profile km 40 to 55, red dashed line) at a depth of 8–11 km. Between the subducted seamount and the ridge (Figure 6a), the décollement parallels the subducting oceanic basement between km 15 to 30 (Figure 6a). At around profile km 9 to 15, the inclination of the décollement is deflected in front of the subducting ridge and steeply trends toward the seafloor, where it crops out at km 9 (Figure 7c). This complex adaptation in the structural level of the décollement is also reflected in the variation of the reflection coefficient (Figure 6a).

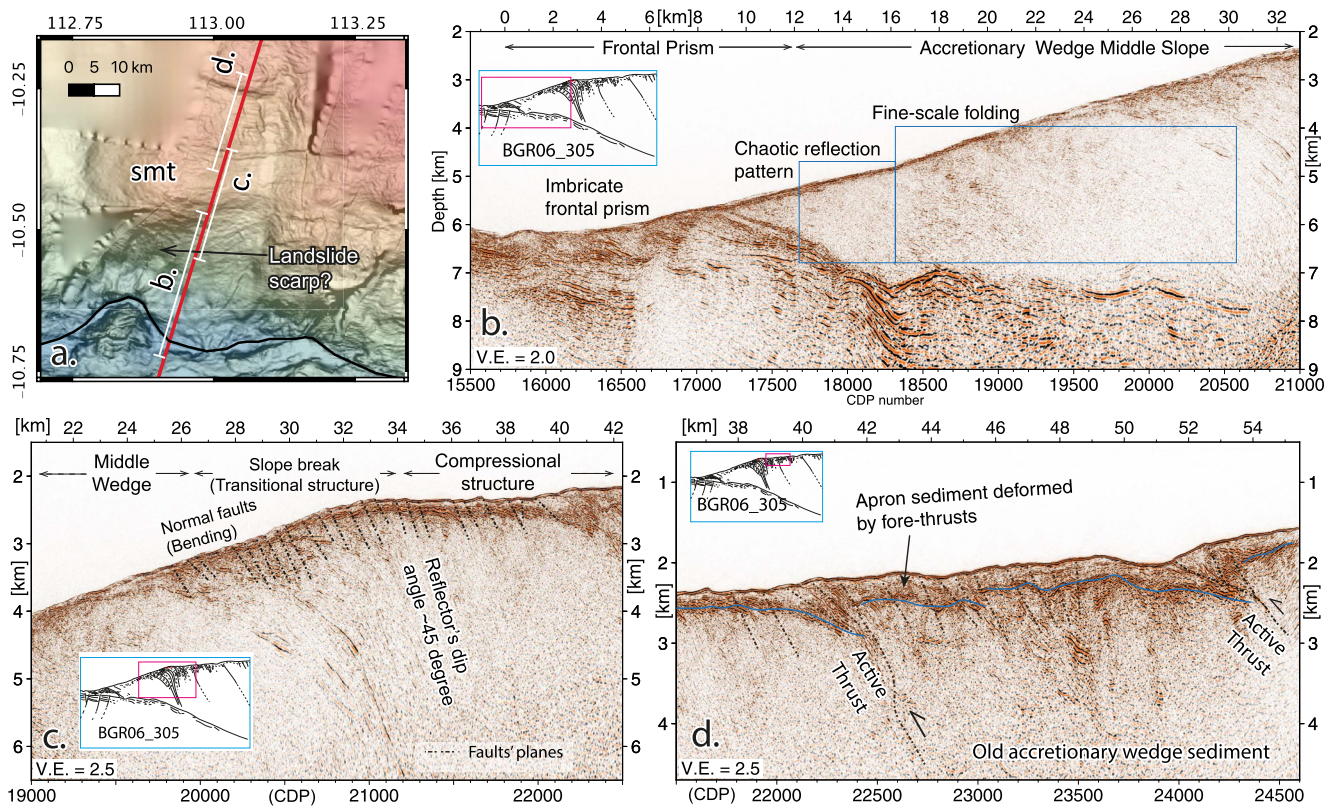


Figure 8. (a) Upper plate seafloor morphology modulated by a subducting seamount adjacent to profile BGR06_305. Seamount subduction induces landsliding and mass wasting on its seaward flank. (b) Close-up view of upper plate seismic signatures in the wake of seamount subduction. The chaotic and fine-scale folding reflections dominate the accretionary wedge middle slope. Frontal sediment accretion results in imbricate thrusting of the frontal prism (km 0–12). (c) Close-up view of the seafloor slope break. Small-scale near-surface normal faults are observed induced by the seafloor curvature, resulting in shallow extension. (d) Close-up view of upper plate structures dominated by active thrusting in front of the seamount. The blue line indicates the basement of the newly deposited apron sediment unit.

4.4. Profile BGR06_305—Offshore Eastern Java

The westernmost profile of our study locates offshore eastern Java, where the oceanic domain features a large number of seamounts on the Roo Rise plateau (Figure 1b & Segment III in Figure 2). The forearc high in this segment reaches a water depth of 750 m and is thus ~2,000 m shallower than offshore Sumbawa (Table 1). The landward deflection of the deformation front by about 50 km (Table 1, Figure 1 & Figure S10 in Supporting Information S1) (Kopp et al., 2006). The incoming plate in the oceanic domain carries ~750 m of well-stratified sediment (Figure 6b, S6 in Supporting Information S1). Oceanic basement and overlying sediments are deformed by bending-induced normal faulting of the oceanic crust as it approaches the trench (Figure 6b, km –10 to 0).

At the deformation front, 40%–50% of the sediment is frontally accreted, resulting in imbricate thrusting within the frontal prism (Figures 6 and 8b, km 0 to 12). Approximately 10–12 km landward of the deformation front, reflectivity within the wedge decreases, marking the transition from the frontal prism (profile km 0–12) to the mature accretionary wedge (Figure 6b). The accretionary wedge is dominated by a chaotic reflection pattern of small-scale reflections (Figures 6b and 8b, profile km 12–16) and fine-scale folding (Figure 8b, profile km 16–30). The seafloor surface slope reaches 8.3° (Figure 6b, km 10–30). A distinct slope break at profile km 33 (Figures 6b and 8c) is associated with a large semi-conical seafloor bulge observed in the bathymetry (smt in Figure 8a). Small-scale, superficial normal faults offset the seafloor (Figure 8c: black dashed lines) to compensate the extension above the bulge. The bulge coincides with a subducted seamount (Xia et al., 2021) on the oceanic crust at a depth of about 7.5 km. Profile BGR06_305 cuts the eastern flank of this ~1,250 km² large seamount (Figure 8a). The seamount and overlying slope break also mark a change in the dipping angle of the plate boundary, which steepens from approximately –2.6° seaward of the slope break to around –10° landward of the seamount (Figure 6b). The décollement runs parallel to the top of the oceanic crust at depths beyond 12 km (profile km 50 and beyond) but starts to deviate from the oceanic basement at the leading flank of the seamount (Figure 6b, profile km 35–50).

Above the seamount and on its landward side (km 33–40), the internal reflectors of the accretionary wedge and forearc high feature a coherent structure with steep dipping angles of about 45° (Figure 6b). A prominent reflector offsets the seafloor at the slope break and cuts through the accretionary wedge down to the plate interface at 9 km depth (Figure 6b). Further landward, we observe seafloor perturbations in both the seismic data (Figure 8d) and the bathymetry (Figure 8a). Two thrust faults are actively deforming the uppermost sedimentary unit (Figures 8a and 8d).

5. Discussion

Although oceanic relief subduction is observed in a large number of accretionary subduction zones (e.g., Bangs et al., 2006; Bell et al., 2010; Tréhu et al., 2012), the comparatively thin oceanic sediment layer (<1,000 m) offshore the Java margin in combination with the significant accretionary wedge make this area unique. The oceanic basement relief is observed to breach the oceanic sediment cover to come into direct contact with the upper plate. This setting provides the opportunity to study the impact of basement relief of different scales on the deformation of the upper plate, the marine forearc mass balance, and the development of the décollement.

The four MCS reflection profiles presented in this study illustrate distinctly different subducting oceanic basement features, ranging from large-scale offshore eastern Java (~40 km wide seamounts, >2.5 km high) to moderate-scale offshore Bali (20–25 km wide seamounts, >2 km high) to subducting ridges off Lombok (4–7 km wide, >1 km high) (Table 2). The easternmost profile offshore Sumbawa shows no significant subducting relief but only minor bending fault scarps (<150 m) and therefore serves as a reference line for the purpose of this discussion. Accordingly, the upper plate structure as well as the trend of the décollement at depth vary between these profiles, documenting the impact of seafloor relief subduction at different scales and different stages of subduction.

5.1. Effects of Seamount Subduction on the Surface Slope and Deformation of the Accretionary Wedge

The subducting oceanic basement relief exerts a first-order control on the seafloor slope. Along strike of the margin, the average seafloor slope across the accretionary wedge increases from 5° offshore Sumbawa to 7.6° offshore Bali and 8.3° offshore Java (Figures 3 and 6, Table 1). This coincides with the increasing size of the subducted basement features and is particularly evident for the Java and Bali profiles (BGR06_305 and BGR06_303), where large to moderate scale seamounts (scale length along the dip: 20–40 km, height >2 km) of the Roo Rise push into the wedge (Figure 1) and the water depth of the forearc high is much shallower (~1,000 m) compared to the eastern profiles.

The two western seismic profiles image the consequences of seamount subduction on the stratigraphy of the accretionary wedge. Above and landward of the seamounts' leading flanks, the sedimentary strata are featured by a steep angle of $\sim 45^\circ$ (Figures 6a and 6b) as they are integrated into the mature portion of the forearc. In front of the largest subducting seamounts observed on profiles BGR06_305 and BGR06_303, active fore-thrusts are observed in both the seismic section and the bathymetry map (Figures 6a and 6b). They cause offsets between 100 and 300 m in the recent sediment apron, increasing to ~500 m in the older accreted sediment (Figures 6b and 8d). We infer that during seamount subduction, its frontal flank pushed the accretionary wedge material landward, and led to the shortening and thickening of the wedge (Figure 9d–f). This is documented by the much shallower water depth (<1,600 m) of the forearc high on the eastern Java and Bali profiles compared to the forearc high elevation (>2,300 m) to the east (Table 1) (Figure 1) as well as by the steeper seafloor slope. The active fore-thrusts, which offset the most recent sedimentary unit and the older accreted material below, result from the thickening and shortening above the seamount's leading flank.

On line BGR06_305, an over-steepened surface slope (8.3° , Table 1) and a shallow basal dip (2.6° , Figure 6b) are observed at the trailing side of a moderate-size seamount. This change in geometry follows the prediction of the classic Coulomb wedge model, which implies an over-critical state of the tape at the trailing flank (Dahlen, 1984; Lallemand & Le Pichon, 1987), facilitating gravitational collapse. Theoretically, the over-steepened surface slope and the shallow basal dip will result in a significant gravitation-driven extensional deformation all over the upper plate at the seamount's trailing edge, given the low strength of the megathrust (Gao & Wang, 2014). The gravity force overcomes the basal shear and leads to pervasive brittle/plastic yielding, and the state of the stress within such a wedge should have the same orientation everywhere (Dahlen, 1984). Evidence of such gravitational collapsing

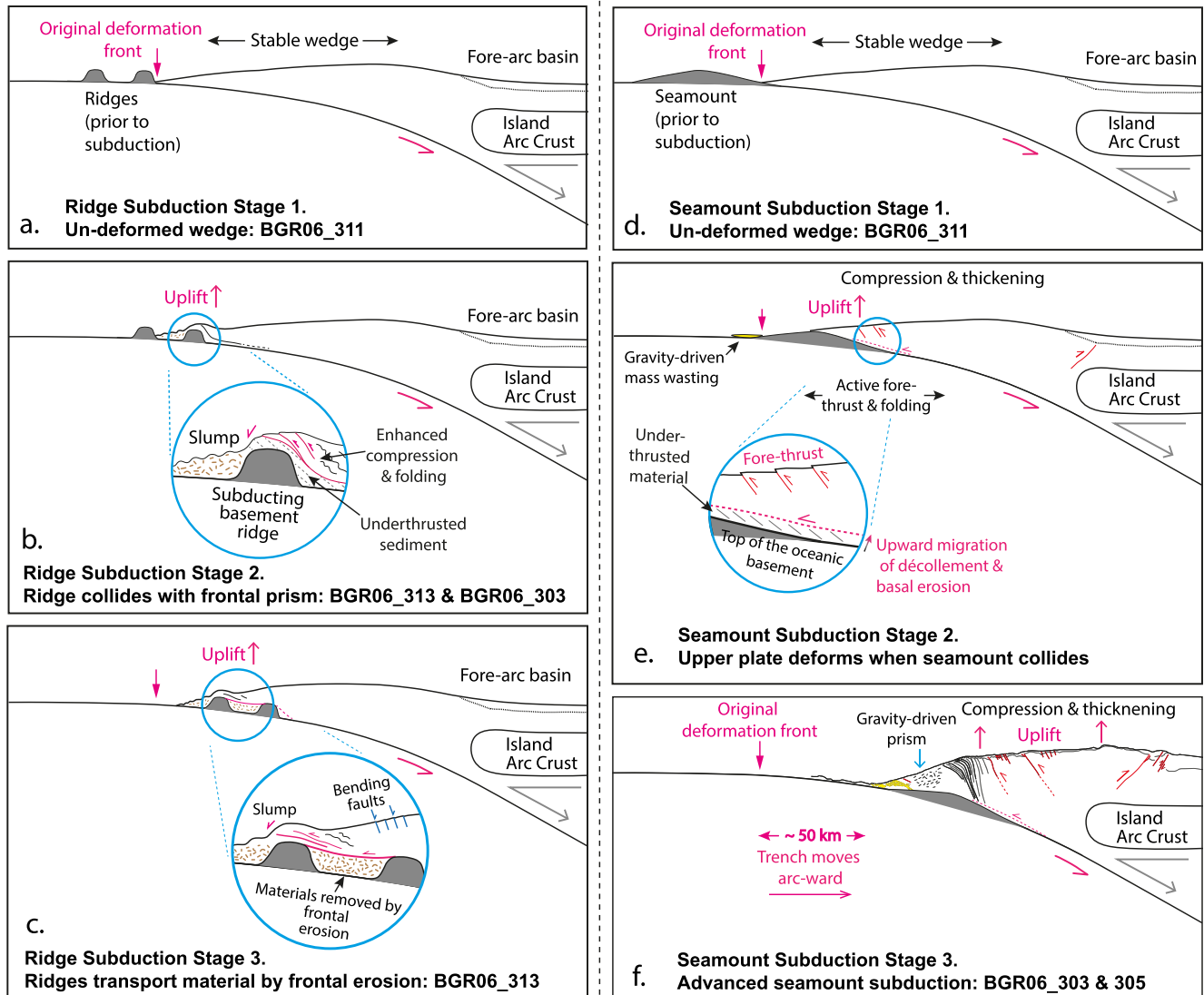


Figure 9. Conceptual sketch of oceanic relief/seamount subduction and associated upper plate deformation showing individual stages of a subducting ridge or seamount. (a) Incipient ridge subduction underneath a stable accretionary wedge. (b) Under-thrusting of the ridge acts as strong teeth and causes uplift and collapsing of the frontal prism. Slumping materials are deposited in the valley at the trailing side of the ridge. (c) The slumping deposit is transported into greater depth as oceanic plate subducts. (d) Incipient seamount subduction underneath a stable accretionary wedge. (e) Seamount under-thrusting causes uplift of the upper plate in front of the seamount and removes upper plate material by basal erosion. (f) Compression and uplift are compensated by fore-thrusts and folding on the seaward side of the prism and by back-thrusting at the transition to the forearc basin. Note that the long-term gravity-driven mass wasting in the wake of relief subduction results in a steep surface slope and a chaotic reflection pattern in the accretionary wedge.

at the seamount's trailing side has been verified in MCS profiles with subducting seamount in North-Ecuadorian margins (Figure 4b in Marcaillou et al., 2016). However, we do not observe widely distributed normal faults or listric faults along the over-steepened middle wedge. Instead, internal structures of this steep wedge taper revealed in seismic lines BGR06_305 and BGR06_303 show intense compressional signatures, like the chaotic and very fine-scale reflectors over the middle wedge at the seamount trailing side (e.g., in BGR06_305, Figure 8b, km 12–30). Only minor normal faults are observed at the surface slope break (Figure 8c, km 24–38).

These observations are related to the continuous and progressive evolution of the upper plate. Compressional debris piles with chaotic reflection signatures often characterize the toe domain of submarine landslides, while extensional fault scarps are only observable at the landslide's headwall domain (Scarselli, 2020). Such extensional

fault scarps will further be eroded by the next gravitationally driven slide (Ruh, 2016) when the seamount subducts deeper. While the normal faults scarps in the headwall domain are transient, re-constructed, and covered by numerous slide episodes, the compressional structural signature in the wake of the subducting seamount is preserved over geologic times (Ruh, 2016). Moreover, the upper plate's tectonic response and topographic expression by the subducting seamount are particularly significant when the seamount is in an early stage of collision close to the trench but will diminish progressively and eventually perish when the seamount reaches a greater depth (e.g., Figures 4e–4h in Ruh et al., 2016). In the end, only minor surface responses are preserved locally above the seamount's top, before the seamount is fully covered by overriding sediment sequences.

The seamounts and basement highs at the early stage of the subduction (e.g., Ridge A in BGR06_313 in this study, and seamount in the North-Ecuadorian margin, Marcaillou et al., 2016) may result in extensive normal faulting and gravitational collapse at their trailing edges when the sediment does not completely bury the seamounts (Ruh, 2016). However, given the convergence rate of the plate margin in Java (67 mm/yr) and the seamount's crest distance to the trench (average 31 km), the seamount observed in BGR06_305 is not anymore at its infant stage of collision. As a consequence of the long-term history of seamount subduction (850 ka) on line BGR06_305 resulting in a series of mass movements over the trailing edge, the stratigraphy above the trailing edge of the seamount is highly disrupted or completely destroyed, resulting in a chaotic reflection pattern dominated by short reflectors (Figures 6 and 8b, km 12 to 30).

A large aspect ratio (height/width ~ 0.2 to 0.3) characterizes subducting ridges close to the trench on the Lombok and Bali profiles (BGR06_313, BGR06_303), which show much steeper flanks than the larger subducting seamounts on the Java and Bali profiles (BGR06_305 and BGR06_303). Deformation in response to the subduction of large aspect ratio features is expressed in intense folding ahead and above the ridge (e.g., Figure 7c, km 8–14), documenting the uplift, deformation, and compression of the sedimentary strata that was formerly composing the frontal prism (Figures 9a–9c). The ridge in profile BGR06_303 shows a local slope of 22° at its trailing edge (Figure 7c, km ~ 7), hosting slumps with chaotic reflection patterns (Figure 7c, km 2 to 6). Comparable steep trailing flanks and mass wasting is observed on the Lombok line as well (Figure 5a, km 0 to 6). This observation indicates that the higher aspect ratio (height/width ~ 0.28 for Ridge A) of the moderate scale basement relief (width of Ridge A < 10 km compared to tens of km for the subducting seamounts) results in enhanced gravitational collapse at the trailing edge. Furthermore, these high aspect ratio reliefs are at an early stage of subduction compared to the seamounts offshore Java and Bali, which are observed at a greater depth so that some “healing” of the lower slope may already have occurred.

In contrast to the three profiles to the west imaging oceanic relief subduction at large to moderate scales, the fourth line offshore Sumbawa (BGR06_311; Figure 3a) shows no comparable subducting structures. Here, the trend of the top of the oceanic basement is only altered by plate-bending induced normal faults, resulting in a small-scale (1–2 km width) segmentation of the subducting oceanic crust with fault throws less than 150 m close to the trench to less than 600 m below the accretionary wedge (Figure 3a). The décollement is able to develop as a spatially continuous feature above the subducting topography, and subducted sediment is observed between the décollement and the top of the oceanic crust (see below). Overall, this profile documents a history of sediment accretion and a stable surface slope of the accretionary wedge not disrupted by significant subducting oceanic basement relief.

5.2. The Evolution of the Décollement in Response to Oceanic Basement Relief Subduction

The subduction of the diverse seafloor topography along the three western profiles (BGR06_305, BGR06_303, and BGR06_313) modifies the reflective nature and structural level of the active décollement. Along the eastern profile BGR06_311, the décollement is spatially continuous and shows a reversed polarity (Figure 3a) and negative reflection coefficient, resulting from a negative impedance contrast indicating juxtaposition of densified, accreted material to underthrust sediment. The décollement marks the top of a 170-m thick unit of subducting sediment, smoothing the smaller scale undulations (< 150 m) of the basement (Figure 3a). This implies that lower plate topography is not in direct contact with the accretionary upper plate. The décollement follows the long-wavelength trend of the subducting slab and does not substantially deviate from the top of the oceanic basement (Figure 3a).

This pattern changes substantially along the neighboring Lombok line (BGR06_313), where Ridges A and B cause undulations in the basement topography by more than 1.5 km in height over a spatial width of less than 7 km (Figure 3b). The décollement is clearly identified by its negative reflection coefficient (Figure 3b), caused

by the negative impedance contrast to the subducting sediment unit underneath. Landward of Ridge B (Figure 3b) the décollement starts to diverge from the top of the oceanic crust (profile km 32), migrates upwards, and follows a shallower trend. This effect is enhanced between Ridges A and B, where the décollement locates ~1.5 km atop the oceanic basement.

On line BGR06_303 offshore Bali, the subducted seamount produces undulations in the basement trend where the basement angle changes significantly over short distances from 1.8° to 8.9° (Figure 6a). This induces a shallowing of the décollement landward of the leading edge of the subducted seamount (around profile km 45–65 in Figure 6a). The décollement reflection amplitude is very weak beyond profile km 35 (Figure 6a), but we deliberately chose not to apply a stronger gain control in order not to heavily manipulate the amplitudes. The décollement is traced 1.2–1.8 km above the top of the oceanic crust but steps down on the trailing flank of the seamount, where it is found less than 600 m above the basement.

The Java profile (BGR06_305) images the largest seamount in our study, but the aspect ratio and hence the changes in subducting basement topography are smaller than on the other lines (Figure 6b). At the leading edge of the seamount, the décollement trends ~1.2 km above the oceanic basement, and can unambiguously be identified by its negative, however weak, reflection coefficient (Figure 6b). Seaward of the seamount, the reflection coefficient of the décollement alternates between positive and negative values, reflecting the impedance contrast between the frontally accreted material in the frontal prism and the underthrust portion of the trench infill (Figure 8b, km 15–20). The décollement polarity in line BGR06_303 is not consistently reversed (Figure 6a, km 15–17) compared to the seafloor reflection, and its polarity alteration is not as distinct as in line 305.

A possible explanation for the alteration of the décollement polarity and impedance contrast at the seamount trailing flank is the local fluid drainage into the upper plate from the under-thrusted sediment or the subducted seamount. Numerical modeling revealed that the porosity of the upper plate material is relatively larger (less consolidated) at the seamount trailing flank compared to its leading side since the upper plate rock at the seamount trailing flank is protected by the stress shadow and becomes less consolidated (Sun, Saffer, & Ellis, 2020). Magnetotelluric (MT) and controlled-source electromagnetic (CSEM) studies in the Hikurangi subduction zone reveal significant fluid drainage from the subducting seamount trailing side, where the upper plate's MCS reflection amplitude is stronger than in adjacent regions (Chesley et al., 2021). In line BGR06_305, we observe a similar stronger amplitude reflection than in the surroundings in the upper plate above the positive polarity décollement reflection (Figure S11 in Supporting Information S1), and it may imply a similar fluid drainage process here as in Hikurangi. We compare the upper plate base P-wave velocity of line BGR06_305 where the large seamount deforms the entire upper plate, to the upper plate v_p of reference line BGR06_313 where the upper plate is affected by subducting ridges in the outer wedge domain. On line BGR06_305 the velocity at the seamount leading flank is higher than the velocity in the reference line at the corresponding distance location (km 36–60), and in contrast, the velocity at the seamount's wake is lower compared to the corresponding location on the reference line (km 12–32) (Figure S13 in Supporting Information S1). This observation indicates a lesser degree of consolidation (high porosity) of the upper plate material at the seamount's wake, and a relatively stronger consolidation (low porosity) at its leading side. However, linking these observations to fluid drainage in Java would require verification from future MT and CSEM studies rather than from seismic amplitude observations alone.

The four profiles in the study area show a systematic decrease of the reflection coefficient away from the trench or as a function of increasing depth (Figures 3 and 6). The gradual loss of high-frequency energy with depth is related to (a) a decrease in the vertical resolution (~1/4 wavelength) which is unable to resolve the under-thrusted sediment strata with finite thickness and (b) the wavelet's peak/maximum amplitude decrease due to the attenuation of the high-frequency signal.

5.3. Subduction Erosion in Java and the Lesser Sunda Margin

The adjustment of the structural level of the décollement has important implications for the mass balance of the forearc. Though subduction erosion has been inferred to be the dominant mode of mass transfer on the Java margin (Kopp et al., 2006), the exact mechanism is still enigmatic. Conventionally, erosion in subduction zones is categorized into three types: (a) subaerial frontal erosion by subducting relief (Von Huene & Lallemand, 1990), (b) basal erosion induced by hydrofracturing or strong basal abrasion (von Huene et al., 2004), or (c) strengthening of the outer wedge during the co-seismic phase of the earthquake cycle (Wang et al., 2010). All three

processes induce thinning and shortening of the upper plate over different timescales, and they are not mutually exclusive from one another.

5.3.1. Tectonic Processes for Frontal Erosion

The ridge subduction close to the trench location in lines BGR06_313 and 303 documents the effect of frontal erosion driven by the subduction of basement topography (Figures 3b, 5a, 6a, and 7c). In front of Ridge A in line BGR06_313 and the ridge close to the trench in line BGR06_303, folding is observed overprinting the accreted upper plate prism (e.g., Figure 7c). The décollement and upper plate internal structure become over-steepened. These observations document the strong compression and clockwise rotation of the accreted sediment at the outer side of the wedge. At the ridges' trailing side, the sedimentary material in line BGR06_313 and 303 show a chaotic internal structure at the toe of the margin, instead of the imbricate structure featuring active thrusting of the accretionary prism or frontal prism as in line BGR06_311 and 305 (Figures 3a and 6b). These observations support that frontal erosion is linked to the subduction of basement topography that will collapse upper plate material and result in slumping at the trailing side of the ridge. As the ridge subducts further, gravitational collapse and slumping generate the re-entrant embayment at the trench. The disintegrated material is deposited in the protected shadow behind the ridge, in the accommodation space of the graben to the next ridge further up-dip (Figure 9b).

In case the collapsed material is again accreted to the upper plate, the material transfer is balanced. Consequently, the identification of the slumping material's under-thrusting and the reduction of the total volume of the accretionary prism are crucial. Fortunately, line BGR06_313 documents the under-thrusted sediment with a thickness of 1.2–1.5 km between Ridges A and B. Since the thickness of the under-thrusted sediment is significantly larger than the sediment deposited on the oceanic crust (<600 m), we infer that more than half of the sediment transported between Ridges A and B is eroded material from the upper plate by means of frontal erosion, which corresponds to $3.4 \sim 4.9 \text{ km}^3$ per 1 km along the arc based on the seismic image (Figure 3a).

Intriguingly, the absolute height/offset of Ridges A and B (1,300–1,600 m) (Figure 3b and Table 2) is larger than for any of the oceanic ridges (800–900 m) observed on the oceanic crust (Figure 1c). We suggest that this effect is related to the oceanic plate bending as the basement scarps in the trench feature an intermediate offset value of 1,000–1,200 m (Figure 5b).

5.3.2. Tectonic Processes for Basal Erosion

The identification of basal erosion from geophysical observations is more difficult to achieve, compared to frontal erosion. Ranero and Von Huene (2000) reported a lens-shaped mass detached below the Costa Rican forearc. Bangs et al. (2006) show that the truncation of the upper plate thrust along the décollement illustrates a missing unit of the upper plate material. Local thinning of the upper plate basement rock observed from the MCS image also indicates a possible local higher basal erosion rate (Marcaillou et al., 2016).

In lines BGR06_303 and 305, we observe a deflection of the décollement, which may be discriminated from the top of the oceanic crust in front of the seamount, and the under-thrusting material between the décollement and the top of the oceanic crust in both PSDM (Figure 6) and PSTM images (Figure S8 in Supporting Information S1). Since the thickness of the under-thrusting material (1.2–1.8 km) in line BGR06_303 is much larger than the oceanic sediment deposit (<600 m), at least half of the under-thrusted sediments are eroded material from the upper plate, which corresponds to $7.8\text{--}10.2 \text{ km}^3$ material per arc length based on the MCS image (Figure 6a). However, how exactly the material is eroded from the base is still enigmatic. Hilde (1983) and Ballance et al. (1989) proposed the chain-saw model which induces enhanced basal abrasion and an elevated plate boundary in front of subducting seamounts, which represents a potential mechanism.

The Coulomb wedge subduction erosion model proposed by Wang et al. (2010) requires the local strengthening of the outer wedge during the co-seismic phase. In terms of the dynamic Coulomb wedge (Wang & Hu, 2006), or a half-space elastic Coulomb stress change model (King et al., 1994), the low-slip shallow part of the megathrust undergoes co-seismic strengthening. However, whether the co-seismic strengthening will induce subduction erosion or thrust faulting aftershocks very much depends on the inter-seismic shear stress status of the megathrust at shallow depth (King et al., 1994). If the shallow megathrust fault stress is high or the coupling rate between two plates is high, the static stress change induced by the earthquake could push the upper plate to reach the brittle/plastic yielding status (e.g., by Mohr-Coulomb criteria) and result in subduction erosion and reverse-faulting along the megathrust or in the upper plate. In contrast, if the shallow interseismic stress is low, the yielding would not occur.

According to the gCMT moment tensor solution catalog, reverse-faulting aftershock activity is absent in the 1994 Java earthquake, and normal faulting aftershocks prevail. Such characteristics indicate an interseismic low-stress status or low coupling rate of the shallow megathrust around the seamount before the 1994 earthquake, similar to the Japan trench ($M \sim 7$) (Mochizuki et al., 2008). This implies that the subduction erosion related to co-seismic strengthening is unlikely to happen.

The landward retreat of the deformation front is as well regarded as a consequence of seamount subduction and has been reproduced by analog modeling (Dominguez et al., 1998). Our MCS images document frontal erosion by subducting ridges in line BGR06_313 as well as basal erosion in front of a seamount in line BGR06_303 where the under-thrusted sedimentary column is thicker than the incoming oceanic sediment. One should note that though the amount of under-thrusting material could be calculated based on the seismic image, the rate of subduction erosion should be rigorously quantified based on paleo-water depth information (Vannucchi et al., 2013; Von Huene & Scholl, 1991), which is currently not available for the Java margin.

While frontal erosion forced by seamount or ridge subduction is commonly observed at subduction systems (Marcaillou et al., 2016; Ranero & Von Huene, 2000), under-thrusting of the slumping material between two ridges is rarely documented in geophysical studies, though the concept has been proposed 30 years ago (Von Huene & Lallemand, 1990). The ~ 1.5 km thick under-thrusting sediment and basal erosion in front of the seamount in line BGR06_303 is also an unexpected feature in the seismic image. One possible explanation is that in the Java case, the seamount is not covered by oceanic sediment and thus directly interacts with the accretionary wedge. In other cases, for example, Costa Rican, Japan Trench, and North-Ecuador, which are erosive margins, the seamounts are interacting with crustal basement rocks (Lallemand & Le Pichon, 1987; Marcaillou et al., 2016; Ranero & Von Huene, 2000). In mature accretionary systems, seamounts are commonly covered or partially covered by oceanic sediment in the accretionary wedge system, so that the subducting seamount's structural impact is limited, as for example, in the Hikurangi subduction zone (Bell et al., 2010). In Nankai, which features a large accretionary wedge, seamount-related basal erosion has also been proposed, but the seismic evidence is different from this study (Bangs et al., 2006). One should also notice that the tectonic response of the seamount subduction varies in different time stages, and each MCS survey carries complex information on the local deformation history.

5.4. Seamount Subduction, Upper Plate Structure and Megathrust Seismogenesis

The role of seamount subduction in the 1994 Java earthquake was previously related to characteristics of the megathrust earthquake, such as the spatial heterogeneity of the co-seismic slip, and the tsunami generation (Abercrombie et al., 2001; Geersen, 2019; Xia et al., 2021).

Based on seafloor bathymetry and teleseismic slip inversion, Abercrombie et al. (2001) proposed that seamount subduction, which is expressed as a bathymetry high on the margin forearc, co-located in the area of the largest slip patch, and facilitated the seismic coupling and earthquake rupture. However, Xia et al. (2021) illustrate that when the subducting seamount is large, significant forearc elevation is generated (a) atop the seamount and (b) at the seamount's leading flank due to strong compression. The seamount observed in line BGR06_305 is located in a region with a relatively low co-seismic slip value of the 1994 earthquake (Xia et al., 2021). Further downdip, in the larger co-seismic slip region, the depth of the décollement (~ 15.6 – 16.2 km) in BGR06_305 is almost identical to that of the line BGR06_313 (~ 15.6 – 16.4 km) at a similar along-strike location (Figure S12 in Supporting Information S1), though the upper plate thickness varies significantly between the two profiles. Based on this observation, no seamount is expected below the shallowest forearc in line BGR06_305 (Figure S12, a in Supporting Information S1). As Xia et al. (2021) have concluded, the seamount observed in seismic line BGR06_305 as well as on the bathymetric map acted as a seismic barrier in the 1994 earthquake and is weakly coupled due to the absence of thrust fault aftershocks. However, due to the limited coverage of the 2D MCS survey, seamount subduction could remain undetected on the western and eastern side of the BGR06_305 profile, and the exact location of seamounts and their roles in the co-seismic rupture remain enigmatic.

Both the 2006 (M_w 7.7) and 1994 (M_w 7.8) Java earthquakes are classified as tsunami earthquakes (Abercrombie et al., 2001; Bilek & Engdahl, 2007). The 2006 event ruptured to the trench, and the 1994 event partially ruptured to the trench. Meanwhile, seismological characteristics (e.g., long rupture duration, small corner frequency, depletion of high-frequency energy, discrepancy between M_w and M_s) are observed from both events.

Conceptual models have been proposed to explain the tsunamigenesis, including (a) shallow co-seismic rupture (0–10 km) favored by the fault rock physical properties (Di Toro et al., 2011; Moore & Saffer, 2001; Oleskevich

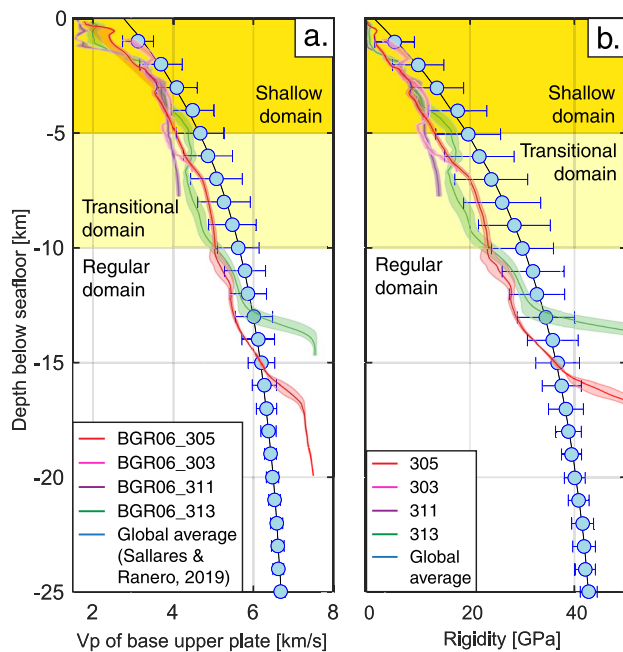


Figure 10. (a) Blue circles and line show global average upper plate base's P-wave velocity as a function of depth, within a 1-km-thick sliding window above the décollement (Sallares & Ranero, 2019). Red, pink, purple, and green lines show upper plate base vp of the MCS lines in this study. (b) Blue circles show global average upper plate rigidity as a function of depth, obtained from rock density and seismic velocity. Other lines show the rigidity in this study.

et al., 1999), and (b) depth-dependent rigidity variations of the upper plate base rock (Sallares & Ranero, 2019).

Though these models are not exclusive from one another, it is essential to distinguish the different consequences implied by each model. Models on the fault rock frictional properties and mechanics predict the *depth extent* of the seismogenic zone in terms of fault rock types and the related weakening mechanisms (e.g., rate-and-state friction law or thermal pressurization) (Di Toro et al., 2011; Dieterich, 1994; Scholz, 1998). A shallow earthquake (0–10 km depth) induces stronger near-surface seafloor displacement and results in a stronger tsunami, compared to an earthquake rupture in the regular depth range (10–40 km depth) (Kanamori, 2014; Lay, 2015). Though petrological and physical property data are missing for the Java subduction zone, we observe that significant portions of the co-seismic slip of the 1994 and 2006 earthquakes locate at shallow depth.

Meanwhile, shallow earthquakes (0–10 km) induce distinct rupture characteristics such as depletion of high-frequency energy, long rupture duration, high co-seismic slip ratio, large discrepancy between M_w and M_s , and lower corner frequency, compared to earthquakes at regular depth (10–40 km) (Kanamori, 2014; Sallares & Ranero, 2019). This discrepancy of rupture characteristics between different depths may be explained by the depth-dependent variation of the upper plate base shear modulus (rigidity) (Sallares & Ranero, 2019).

Following this concept, we calculate the rigidity at the upper plate base, relative rupture duration, and relative slip ratio of the potential earthquake based on the MCS and OBS vp models of the four seismic lines (Figures S3–6 in Supporting Information S1), and compare them with the world-wide average trend (Figure 10 & S14 in Supporting Information S1), which is based on 48 published seismic velocity models (for calculation method and global data compilation, please refer to Sallares & Ranero, 2019).

First, we found that the upper plate base vp of all four lines follows the trend of the systematic depth-dependent law of the upper plate rigidity which explains the shallow and the deeper earthquakes' different rupture characteristics (Sallares & Ranero, 2019). Secondly, the upper plate rigidity of the four lines systematically deviated from the global trend by -5 to -10 GPa from the shallow to regular depth domain (Figure 10). Consequentially, the theoretically calculated co-seismic slip ratio and the relative rupture duration are larger than global references at all corresponding depths (Figure S14 in Supporting Information S1). This relatively low value of the upper plate base vp and rigidity is a common feature in the Java margin, *independent of seamount subduction* (Figure 10).

6. Conclusions

1. From the bathymetry and MCS surveys in the eastern Java margin, distinct oceanic relief is observed: (a) on the oceanic seafloor prior to subduction, and (b) being subducted underneath the overriding plate on the submerged plate interface. Along the margin strike, these oceanic basement highs feature a large diversity in scales and shapes, including large conical seamounts (diameter up to 40 km), high aspect ratio linear-shape ridges (height/width >0.25), and oceanic plate bending normal faults with small offsets (vertical throw <150 m).
2. In the accretionary wedge of the outer marine forearc, structural impacts from subducting seamounts and ridges share similar patterns and might share as well a scale-independent deformation mechanism. Enhanced compression, including active thrust-faulting and folding, is observed at the subducting relief's leading edges to compensate for the change of the basal dip and the shortening at the seaward side of the wedge following the prediction from the Coulomb wedge theory. In contrast, at the trailing edge of the relief, the overriding plate features a structureless reflection signature. This pattern likely results from numerous gravitational slumps at the relief's trailing side in its long-term subduction history until they are fully buried by the overriding sediment sequence.

3. The larger seamounts and linear ridges breach the relatively thin sediment cover (<500 m) on the oceanic crust. Upon collision with the upper plate and subsequent subduction, they affect the upper plate mass balance by subduction erosion. Offshore Lombok, line BGR06_313 documents frontal erosion and the under-thrusting of eroded material between two subducting ridges. Offshore Bali, line BGR06_303 documents basal erosion of under-thrusting material in front of a subducted seamount. These erosional processes permanently remove accreted material to a greater depth.
4. Subducting oceanic relief will lead to a substantial structural response on the upper plate if the height of the relief is larger than the thickness of the pelagic and terrestrial sediment on the oceanic plate prior to subduction. Underneath the frontal part of the accretionary wedge offshore Sumbawa (BGR06_311), small bending fault scarps (<150 m) are smoothed by the 170 m thick under-thrusting sediment. From bathymetry and subsurface observations, no indication of severe upper plate deformation by the oceanic bending fault scarps is observed here.
5. Two tsunami earthquakes occurred at the Java margin in the past 30 years. By analyzing the P-wave velocity structure based on MCS and OBS velocity inversion, systematic deviations of the upper plate base v_p (−0.5 to −1 km/s) and rigidity (−5 to −10 GPa) are found on all four seismic lines from 0 to 15 km depth below seafloor, with and without the influence of seamount subduction. The rigidity reduction in the depth range of the seismogenic zone may help explain the longer rupture duration, lower corner frequency, and higher-than-expected tsunami run-ups of the 1994 and 2006 tsunami earthquakes.

Conflict of Interest

The authors declare no conflicts of interest relevant to this study.

Data Availability Statement

The multi-channel seismic data were processed with Schlumberger's seismic processing suite Omega2 (<https://www.software.slb.com/products/omega>) via academic license and Seismic Unix - open-source software package (Stockwell, 1999) for seismic research and processing, Center for Wave Phenomena, Colorado School of Mines (<https://wiki.seismic-unix.org/start>). The bathymetry figure and the seismic images in the study are plotted by the Generic Mapping Tools (GMT) (Wessel et al., 2013) version 5.4 available at <https://www.genericmapping-tools.org/>, and QGIS (QGIS.org, 2023) version 3.16 LTR at <https://qgis.org/en/site/>.

All depth-migrated multi-channel seismic profiles (BGR06_303, BGR06_305, BGR06_311, and BGR06_313) are archived and accessible from the online repository Zenodo (Xia et al., 2022a) at <https://doi.org/10.5281/zenodo.7973111>. The merged multi-beam bathymetric data from RV SONNE cruise SO190 is archived and accessible on the Zenodo online repository (Xia et al., 2022b) at <https://doi.org/10.5281/zenodo.7417701>. The global bathymetry and topography dataset GEBCO (GEBCO, 2020) is available at (<https://www.gebco.net/>).

Acknowledgments

Y. Xia acknowledges funding from the China Scholarship Council (Grant 201506400067), GEOMAR Helmholtz Centre for Ocean Research Kiel, and National Natural Science Foundation of China (Grant 42306095). R/V SONNE cruise SO190 and the SINDBAD project were funded by the German Federal Ministry of Education and Research (BMBF) under Grants 03G0190A and 03G0190B. We thank editor Isabelle Manighetti, the associated editor, and two anonymous reviewers for valuable comments and suggestions that greatly improved the manuscript. Open Access funding enabled and organized by Projekt DEAL.

References

- Abercrombie, R. E., Antolik, M., Felzer, K., Ekstrom, G., & Ekström, G. (2001). The 1994 Java tsunami earthquake: Slip over a subducting seamount. *Journal of Geophysical Research*, 106(B4), 6595–6607. <https://doi.org/10.1029/2000jb900403>
- Ballance, P. F., Scholl, D. W., Vallier, T. L., Stevenson, A. J., Ryan, H., & Herzer, R. H. (1989). Subduction of a late cretaceous seamount of the Louisville ridge at the Tonga trench: A model of normal and accelerated tectonic erosion. *Tectonics*, 8(5), 953–962. <https://doi.org/10.1029/TC008i005p00953>
- Bangs, N. L. B., Gulick, S. P. S., & Shipley, T. H. (2006). Seamount subduction erosion in the Nankai Trough and its potential impact on the seismogenic zone. *Geology*, 34(8), 701. <https://doi.org/10.1130/G22451.1>
- Barker, D. H. N., Henrys, S., Caratori Tontini, F., Barnes, P. M., Bassett, D., Todd, E., & Wallace, L. (2018). Geophysical constraints on the relationship between seamount subduction, slow slip, and tremor at the North Hikurangi subduction zone, New Zealand. *Geophysical Research Letters*, 45(23), 12804–12813. <https://doi.org/10.1029/2018GL080259>
- Bell, R., Holden, C., Power, W., Wang, X., & Downes, G. (2014). Hikurangi margin tsunami earthquake generated by slow seismic rupture over a subducted seamount. *Earth and Planetary Science Letters*, 397, 1–9. <https://doi.org/10.1016/j.epsl.2014.04.005>
- Bell, R., Sutherland, R., Barker, D. H. N., Henrys, S., Bannister, S., Wallace, L., & Beavan, J. (2010). Seismic reflection character of the Hikurangi subduction interface, New Zealand, in the region of repeated Gisborne slow slip events. *Geophysical Journal International*, 180(1), 34–48. <https://doi.org/10.1111/j.1365-246X.2009.04401.x>
- Bilek, S. L., & Engdahl, E. R. (2007). Rupture characterization and aftershock relocations for the 1994 and 2006 tsunami earthquakes in the Java subduction zone. *Geophysical Research Letters*, 34(20), L20311. <https://doi.org/10.1029/2007GL031357>
- Bock, Y., Prawirodirdjo, L., Genrich, J. F., Stevens, C. W., McCaffrey, R., Subarya, C., et al. (2003). Crustal motion in Indonesia from global positioning system measurements. *Journal of Geophysical Research: Solid Earth*, 108(B8), 2367. <https://doi.org/10.1029/2001jb000324>
- Bonnet, G., Agard, P., Angiboust, S., Fournier, M., & Omrani, J. (2019). No large earthquakes in fully exposed subducted seamount. *Geology*, 47(5), 407–410. <https://doi.org/10.1130/G45564.1>

- Brune, S., Ladage, S., Babeyko, A. Y., Müller, C., Kopp, H., & Sobolev, S. V. (2010). Submarine landslides at the eastern Sunda margin: Observations and tsunami impact assessment. *Natural Hazards*, 54(2), 547–562. <https://doi.org/10.1007/s11069-009-9487-8>
- Caress, D. W., & Chayes, D. N. (1996). Improved processing of Hydrosweep DS multibeam data on the R/V Maurice Ewing. *Marine Geophysical Researches*, 18(6), 631–650. <https://doi.org/10.1007/BF00313878>
- Chesley, C., Naif, S., Key, K., & Bassett, D. (2021). Fluid-rich subducting topography generates anomalous forearc porosity. *Nature*, 595(7866), 255–260. <https://doi.org/10.1038/s41586-021-03619-8>
- Cloos, M. (1992). Thrust-type subduction-zone earthquakes and seamount asperities - a physical model for seismic rupture. *Geology*, 20(7), 601–604. [https://doi.org/10.1130/0091-7613\(1992\)020<0601:Ttszea>2.3.CO;2](https://doi.org/10.1130/0091-7613(1992)020<0601:Ttszea>2.3.CO;2)
- Cloos, M., & Shreve, R. L. (1996). Shear-zone thickness and the seismicity of Chilean- and Marianas-type subduction zones. *Geology*, 24(2), 107–110. [https://doi.org/10.1130/0091-7613\(1996\)024<0107:SZTATS>2.3.CO;2](https://doi.org/10.1130/0091-7613(1996)024<0107:SZTATS>2.3.CO;2)
- Dahlen, F. A. (1984). Noncohesive critical Coulomb wedges: An exact solution. *Journal of Geophysical Research*, 89(B12), 10125–10133. <https://doi.org/10.1029/JB089iB12p10125>
- Davidson, S. R., Barnes, P. M., Pettinga, J. R., Nicol, A., Mountjoy, J. J., & Henrys, S. A. (2020). Conjugate strike-slip faulting across a subduction front driven by incipient seamount subduction. *Geology*, 48(5), 493–498. <https://doi.org/10.1130/G47154.1>
- Dieterich, J. (1994). A constitutive law for rate of earthquake production and its application to earthquake clustering. *Journal of Geophysical Research*, 99(B2), 2601–2618. <https://doi.org/10.1029/93JB02581>
- Di Toro, G., Han, R., Hirose, T., De Paola, N., Nielsen, S., Mizoguchi, K., et al. (2011). Fault lubrication during earthquakes. *Nature*, 471(7339), 494–499. <https://doi.org/10.1038/nature09838>
- Dominguez, S., Lallemand, S. E., Malavieille, J., & Von Huene, R. (1998). Upper plate deformation associated with seamount subduction. *Tectonophysics*, 293(3–4), 207–224. [https://doi.org/10.1016/S0040-1951\(98\)00086-9](https://doi.org/10.1016/S0040-1951(98)00086-9)
- Edwards, J. H., Kluesner, J. W., Silver, E. A., Brodsky, E. E., Brothers, D. S., Bangs, N. L., et al. (2018). Corrugated megathrust revealed offshore from Costa Rica. *Nature Geoscience*, 11(3), 197–202. <https://doi.org/10.1038/s41561-018-0061-4>
- Gao, X., & Wang, K. (2014). Strength of stick-slip and creeping subduction megathrusts from heat flow observations. *Science*, 345(6200), 1038–1041. <https://doi.org/10.1126/science.1255487>
- GEBCO Bathymetric Compilation Group. (2020). The GEBCO_2020 Grid - A continuous terrain model of the global oceans and land [Dataset]. British Oceanographic Data Centre, National Oceanography Centre, NERC. <https://doi.org/10.5285/836f016a-33be-6ddc-e053-6c86abc0788e>
- Geersen, J. (2019). Sediment-starved trenches and rough subducting plates are conducive to tsunami earthquakes. *Tectonophysics*, 762(March), 28–44. <https://doi.org/10.1016/j.tecto.2019.04.024>
- Guitton, A., & Verschuur, D. J. (2004). Adaptive subtraction of multiples using the L1-norm. *Geophysical Prospecting*, 52(1), 27–38. <https://doi.org/10.1046/j.1365-2478.2004.00401.x>
- Hall, R. (2002). Cenozoic geological and plate tectonic evolution of SE Asia and the SW Pacific: Computer-based reconstructions, model and animations. *Journal of Asian Earth Sciences*, 20(4), 353–431. [https://doi.org/10.1016/S1367-9120\(01\)00069-4](https://doi.org/10.1016/S1367-9120(01)00069-4)
- Hall, R., & Smyth, H. R. (2008). Cenozoic arc processes in Indonesia: Identification of the key influences on the stratigraphic record in active volcanic arcs. *Special Paper of the Geological Society of America*, 436(03), 27–54. [https://doi.org/10.1130/2008.2436\(03](https://doi.org/10.1130/2008.2436(03)
- Hamilton, W. B. (1988). Plate tectonics and island arcs. *Special Paper of the Geological Society of America*, 253(10), 113–137. <https://doi.org/10.1130/SPE253-p113>
- Han, S., Carbotte, S. M., Canales, J. P., Nedimović, M. R., & Carton, H. (2018). Along-trench structural variations of the subducting Juan de Fuca plate from multichannel seismic reflection imaging. *Journal of Geophysical Research: Solid Earth*, 123(4), 3122–3146. <https://doi.org/10.1002/2017JB015059>
- Heine, C., Dietmar Müller, R., & Gaina, C. (2004). Reconstructing the lost eastern tethys ocean basin: Convergence history of the se Asian margin and marine gateways. *Geophysical Monograph Series*, 149, 37–54. <https://doi.org/10.1029/149GM03>
- Hilde, T. W. C. (1983). Sediment subduction versus accretion around the pacific. *Tectonophysics*, 99(2–4), 381–397. [https://doi.org/10.1016/0040-1951\(83\)90114-2](https://doi.org/10.1016/0040-1951(83)90114-2)
- Hoernle, K., Hauff, F., Werner, R., Van Den Bogaard, P., Gibbons, A. D., Conrad, S., & Müller, R. D. (2011). Origin of Indian Ocean seamount province by shallow recycling of continental lithosphere. *Nature Geoscience*, 4(12), 883–887. <https://doi.org/10.1038/ngeo1331>
- Hühnerbach, V., Masson, D. G., Bohrmann, G., Bull, J. M., & Weinrebe, W. (2005). Deformation and submarine landsliding caused by seamount subduction beneath the Costa Rica continental margin - New insights from high-resolution sidescan sonar data. *Geological Society Special Publication*, 244(1), 195–205. <https://doi.org/10.1144/GSL.SP.2005.244.01.12>
- Kanamori, H. (2014). The diversity of large earthquakes and its implications for hazard mitigation. *Annual Review of Earth and Planetary Sciences*, 42(1), 7–26. <https://doi.org/10.1146/annurev-earth-060313-055034>
- Karig, D. E., Moore, G. F., Curraj, J. R., & Lawrence, M. B. (1980). Morphology and shallow structure of the lower trench slope off Nias Island, Sunda arc. *The Tectonic and Geologic Evolution of Southeast Asian Seas and Islands. Part 1*, 23, 179–208. <https://doi.org/10.1029/gm023p0179>
- King, G. C. P., Stein, R. S., & Lin, J. (1994). Static stress changes and the triggering of earthquakes. *Bulletin of the Seismological Society of America*, 84(3), 935–953. [https://doi.org/10.1016/0148-9062\(95\)94484-2](https://doi.org/10.1016/0148-9062(95)94484-2)
- Kodaira, S., Fujie, G., Yamashita, M., Sato, T., Takahashi, T., & Takahashi, N. (2014). Seismological evidence of mantle flow driving plate motions at a palaeo-spreading centre. *Nature Geoscience*, 7(5), 371–375. <https://doi.org/10.1038/ngeo2121>
- Kodaira, S., Takahashi, N., Nakanishi, A., Miura, S., & Kaneda, Y. (2000). Subducted seamount imaged in the rupture zone of the 1946 Nankaido earthquake. *Science*, 289(5476), 104–106. <https://doi.org/10.1126/science.289.5476.104>
- Kopp, H. (2011). The Java convergent margin: Structure, seismogenesis and subduction processes. *Geological Society Special Publication*, 355(1), 111–137. <https://doi.org/10.1144/SP355.6>
- Kopp, H., Flueh, E., Petersen, C., Weinrebe, W., Wittwer, A., & Scientists, M. (2006). The Java margin revisited: Evidence for subduction erosion off Java. *Earth and Planetary Science Letters*, 242(1–2), 130–142. <https://doi.org/10.1016/j.epsl.2005.11.036>
- Kopp, H., Hindle, D., Klaeschen, D., Oncken, O., Reichert, C., & Scholl, D. (2009). Anatomy of the western Java plate interface from depth-migrated seismic images. *Earth and Planetary Science Letters*, 288(3–4), 399–407. <https://doi.org/10.1016/j.epsl.2009.09.043>
- Krabbenhoft, A., Weinrebe, R. W., Kopp, H., Flueh, E. R., Ladage, S., Papenberg, C., et al. (2010). Bathymetry of the Indonesian Sunda margin-relating morphological features of the upper plate slopes to the location and extent of the seismogenic zone. *Natural Hazards and Earth System Science*, 10(9), 1899–1911. <https://doi.org/10.5194/nhess-10-1899-2010>
- Lallemand, S., Culotta, R., & Von Huene, R. (1989). Subduction of the Daiichi Kashima seamount in the Japan trench. *Tectonophysics*, 160(1–4), 231–241. [https://doi.org/10.1016/0040-1951\(89\)90393-4](https://doi.org/10.1016/0040-1951(89)90393-4)
- Lallemand, S., & Le Pichon, X. (1987). Coulomb wedge model applied to the subduction of seamounts in the Japan Trench. *Geology*, 15(11), 1065–1069. [https://doi.org/10.1130/0091-7613\(1987\)15<1065:CWMATT>2.0.CO;2](https://doi.org/10.1130/0091-7613(1987)15<1065:CWMATT>2.0.CO;2)

- Laursen, J., Scholl, D. W., & Von Huene, R. (2002). Neotectonic deformation of the central Chile margin: Deepwater forearc basin formation in response to hot spot ridge and seamount subduction. *Tectonics*, 21(5), 21–227. <https://doi.org/10.1029/2001tc901023>
- Lay, T. (2015). The surge of great earthquakes from 2004 to 2014. *Earth and Planetary Science Letters*, 409, 133–146. <https://doi.org/10.1016/j.epsl.2014.10.047>
- Lüschen, E., Müller, C., Kopp, H., Engels, M., Lutz, R., Planert, L., et al. (2011). Structure, evolution and tectonic activity of the eastern Sunda forearc, Indonesia, from marine seismic investigations. *Tectonophysics*, 508(1–4), 6–21. <https://doi.org/10.1016/j.tecto.2010.06.008>
- Ma, B., Geersen, J., Klaeschen, D., Contreras-Reyes, E., Riedel, M., Xia, Y., et al. (2023). Impact of the Iquique Ridge on structure and deformation of the north Chilean subduction zone. *Journal of South American Earth Sciences*, 124(Febuary), 104262. <https://doi.org/10.1016/j.jsames.2023.104262>
- Marcaillou, B., Collot, J. Y., Ribodetti, A., d'Acremont, E., Mahamat, A. A., & Alvarado, A. (2016). Seamount subduction at the North-Ecuadorian convergent margin: Effects on structures, inter-seismic coupling and seismogenesis. *Earth and Planetary Science Letters*, 433(October 2017), 146–158. <https://doi.org/10.1016/j.epsl.2015.10.043>
- Marcaillou, B., Klingelhoefer, F., Laurencin, M., Lebrun, J. F., Laigle, M., Lallemand, S., et al. (2021). Pervasive detachment faults within the slow spreading oceanic crust at the poorly coupled Antilles subduction zone. *Communications Earth and Environment*, 2(1), 203. <https://doi.org/10.1038/s43247-021-00269-6>
- Martínez-Loriente, S., Sallarès, V., Ranero, C. S., Ruh, J. B., Barckhausen, U., Grevemeyer, I., & Bangs, N. (2019). Influence of incoming plate relief on overriding plate deformation and earthquake nucleation: Cocos ridge subduction (Costa Rica). *Tectonics*, 38(12), 4360–4377. <https://doi.org/10.1029/2019TC005586>
- McNeill, L. C., & Henstock, T. J. (2014). Forearc structure and morphology along the Sumatra-Andaman subduction zone. *Tectonics*, 33(2), 112–134. <https://doi.org/10.1002/2012TC003264>
- Mochizuki, K., Yamada, T., Shinohara, M., Yamanaka, Y., & Kanazawa, T. (2008). Weak interplate coupling by seamounts and repeating M ~7 earthquakes. *Science*, 321(5893), 1194–1197. <https://doi.org/10.1126/science.1160250>
- Moore, G. F., Curray, J. R., & Emmel, F. J. (1982). Sedimentation in the Sunda trench and forearc region. *Geological Society Special Publication*, 10(1), 245–258. <https://doi.org/10.1144/GSL.SP.1982.010.01.16>
- Moore, G. F., Curray, J. R., Moore, D. G., & Karig, D. E. (1980). Variations in geologic structure along the Sunda fore arc, northeastern Indian Ocean (figure 1). *The Tectonic and Geologic Evolution of Southeast Asian Seas and Islands. Part 1*(23), 145–160. <https://doi.org/10.1029/gm023p0145>
- Moore, J. C., & Saffer, D. (2001). Updip limit of the seismogenic zone beneath the accretionary prism of southwest Japan: An effect of diagenetic to low-grade metamorphic processes and increasing effective stress. *Geology*, 29(2), 183–186. [https://doi.org/10.1130/0091-7613\(2001\)029<0183:Ulotsz>2.0.Co;2](https://doi.org/10.1130/0091-7613(2001)029<0183:Ulotsz>2.0.Co;2)
- Morton, E. A., Bilek, S. L., & Rowe, C. A. (2018). Newly detected earthquakes in the Cascadia subduction zone linked to seamount subduction and deformed upper plate. *Geology*, 46(11), 943–946. <https://doi.org/10.1130/G45354.1>
- Müller, C., Kopp, H., Djajadihardja, Y. S., Barckhausen, U., Ehrhardt, A., Engels, M., et al. (2008). From subduction to collision: The Sunda-Banda Arc transition. *Eos*, 89(6), 49–50. <https://doi.org/10.1029/2008EO060001>
- Müller, C., & Neben, S. (2006). Research Cruise SO190 Leg 1, SINDBAD, Seismic and geoacoustic investigations along the Sunda-Banda Arc transition (Seismische und geokustische Untersuchungen entlang des Übergangs vom Sunda-zum Banda-Bogen) with RV SONNE, Jakarta, Indonesia 09th October. *Bundesanstalt Für Geowissenschaften Und Rohstoffe, November*, 142. https://doi.org/10.2312/cr_so190_1
- Oleskevich, D. A., Hyndman, R. D., & Wang, K. (1999). The updip and downdip limits to great subduction earthquakes: Thermal and structural models of Cascadia, south Alaska, SW Japan, and Chile. *Journal of Geophysical Research*, 104(B7), 14965–14991. <https://doi.org/10.1029/1999jb900060>
- Planert, L., Kopp, H., Lueschen, E., Mueller, C., Flueh, E. R., Shulgin, A., et al. (2010). Lower plate structure and upper plate deformational segmentation at the Sunda-Banda arc transition, Indonesia. *Journal of Geophysical Research*, 115(B8), B08107. <https://doi.org/10.1029/2009JB006713>
- QGIS.org. (2023). QGIS geographic information system [Software]. QGIS Association. Retrieved from <http://www.qgis.org>
- Ranero, C. R., Reston, T. J., Belykh, I., & Gnibidenko, H. (1997). Reflective oceanic crust formed at a fast-spreading center in the Pacific. *Geology*, 25(6), 499–502. [https://doi.org/10.1130/0091-7613\(1997\)025<0499:ROCFAA>2.3.CO;2](https://doi.org/10.1130/0091-7613(1997)025<0499:ROCFAA>2.3.CO;2)
- Ranero, C. R., & Von Huene, R. (2000). Subduction erosion along the Middle America convergent margin. *Nature*, 404(6779), 748–752. <https://doi.org/10.1038/35008046>
- Ruh, J. B. (2016). Submarine landslides caused by seamounts entering accretionary wedge systems. *Terra Nova*, 28(3), 163–170. <https://doi.org/10.1111/ter.12204>
- Ruh, J. B., Sallarès, V., Ranero, C. R., & Gerya, T. (2016). Crustal deformation dynamics and stress evolution during seamount subduction: High-resolution 3-D numerical modeling. *Journal of Geophysical Research: Solid Earth*, 121(9), 6880–6902. <https://doi.org/10.1002/2016JB013250>
- Sallarès, V., & Ranero, C. R. (2019). Upper-plate rigidity determines depth-varying rupture behaviour of megathrust earthquakes. *Nature*, 576(7785), 96–101. <https://doi.org/10.1038/s41586-019-1784-0>
- Scarselli, N. (2020). Submarine landslides - Architecture, controlling factors and environments. A summary. In *Regional geology and tectonics: Principles of geologic analysis volume 1: Principles of geologic analysis. BV*. <https://doi.org/10.1016/B978-0-444-64134-2.00015-8>
- Scholz, C. H. (1998). Earthquakes and friction laws. *Nature*, 391(6662), 37–42. <https://doi.org/10.1038/34097>
- Scholz, C. H., & Small, C. (1997). The effect of seamount subduction on seismic coupling. *Geology*, 25(6), 487. [https://doi.org/10.1130/0091-7613\(1997\)025<0487:TEOSSO>2.3.CO;2](https://doi.org/10.1130/0091-7613(1997)025<0487:TEOSSO>2.3.CO;2)
- Seton, M., Müller, R. D., Zahirovic, S., Williams, S., Wright, N. M., Cannon, J., et al. (2020). A global data set of present-day oceanic crustal age and seafloor spreading parameters. *Geochemistry, Geophysics, Geosystems*, 21(10), 0–3. <https://doi.org/10.1029/2020GC009214>
- Shulgin, A., Kopp, H., Mueller, C., Planert, L., Lueschen, E., Flueh, E. R., & Djajadihardja, Y. (2011). Structural architecture of oceanic plateau subduction offshore Eastern Java and the potential implications for geohazards. *Geophysical Journal International*, 184(1), 12–28. <https://doi.org/10.1111/j.1365-246X.2010.04834.x>
- Stockwell, J. W. (1999). The CWP/SU: Seismic Un(*)x package [software]. *Computers & Geosciences*, 25(4), 415–419. [https://doi.org/10.1016/S0098-3004\(98\)00145-9](https://doi.org/10.1016/S0098-3004(98)00145-9)
- Sun, T., Ellis, S., & Saffer, D. (2020). Coupled evolution of deformation, pore fluid pressure, and fluid flow in shallow subduction forearcs. *Journal of Geophysical Research: Solid Earth*, 125(3), 1–26. <https://doi.org/10.1029/2019JB019101>
- Sun, T., Saffer, D., & Ellis, S. (2020). Mechanical and hydrological effects of seamount subduction on megathrust stress and slip. *Nature Geoscience*, 13(3), 249–255. <https://doi.org/10.1038/s41561-020-0542-0>

- Tan, H., Gao, X., Wang, K., Gao, J., & He, J. (2022). Hidden roughness of subducting seafloor and implications for megathrust seismogenesis: Example from northern Manila trench. *Geophysical Research Letters*, 49(17). <https://doi.org/10.1029/2022GL100146>
- Timm, C., Bassett, D., Graham, I. J., Leybourne, M. I., De Ronde, C. E. J., Woodhead, J., et al. (2013). Louisville seamount subduction and its implication on mantle flow beneath the central Tonga-Kermadec arc. *Nature Communications*, 4(1), 1720. <https://doi.org/10.1038/ncomms2702>
- Todd, E. K., Schwartz, S. Y., Mochizuki, K., Wallace, L. M., Sheehan, A. F., Webb, S. C., et al. (2018). Earthquakes and Tremor linked to seamount subduction during shallow slow slip at the Hikurangi margin, New Zealand. *Journal of Geophysical Research: Solid Earth*, 123(8), 6769–6783. <https://doi.org/10.1029/2018JB016136>
- Tregoning, P., Brunner, F. K., Bock, Y., Puntodewo, S. S. O., McCaffrey, R., Genrich, J. F., et al. (1994). First geodetic measurement of convergence across the Java Trench. *Geophysical Research Letters*, 21(19), 2135–2138. <https://doi.org/10.1029/94GL01856>
- Tréhu, A. M., Blakely, R. J., & Williams, M. C. (2012). Subducted seamounts and recent earthquakes beneath the central cascadia forearc. *Geology*, 40(2), 103–106. <https://doi.org/10.1130/G32460.1>
- Vannucchi, P., Sak, P. B., Morgan, J. P., Ohkushi, K., & Ujiie, K. (2013). Rapid pulses of uplift, subsidence, and subduction erosion offshore central America: Implications for building the rock record of convergent margins. *Geology*, 41(9), 995–998. <https://doi.org/10.1130/G34355.1>
- Van Rijnsing, E., Funicello, F., Corbi, F., & Lallemand, S. (2019). Rough subducting seafloor reduces interseismic coupling and mega-earthquake occurrence: Insights from analogue models. *Geophysical Research Letters*, 46(6), 3124–3132. <https://doi.org/10.1029/2018GL081272>
- Verschuur, D. J., Berkhout, A. J., & Wapenaar, C. P. A. (1992). Adaptive surface-related multiple elimination. *Geophysics*, 57(9), 1166–1177. <https://doi.org/10.1190/1.1443330>
- Von Huene, R., & Lallemand, S. (1990). Tectonic erosion along the Japan and Peru convergent margins. *Geological Society of America Bulletin*, 102(6), 704–720. [https://doi.org/10.1130/0016-7606\(1990\)102<0704:TEATJA>2.3.CO;2](https://doi.org/10.1130/0016-7606(1990)102<0704:TEATJA>2.3.CO;2)
- Von Huene, R., Ranero, C. R., & Vannucchi, P. (2004). Generic model of subduction erosion. *Geology*, 32(10), 913. <https://doi.org/10.1130/G20563.1>
- Von Huene, R., & Scholl, D. W. (1991). Observations at convergent margins concerning sediment subduction, subduction erosion, and the growth of continental crust. *Reviews of Geophysics*, 29(3), 279. <https://doi.org/10.1029/91RG00969>
- Wang, K., & Bilek, S. L. (2011). Do subducting seamounts generate or stop large earthquakes? *Geology*, 39(9), 819–822. <https://doi.org/10.1130/G31856.1>
- Wang, K., & Bilek, S. L. (2014). Invited review paper: Fault creep caused by subduction of rough seafloor relief. *Tectonophysics*, 610, 1–24. <https://doi.org/10.1016/j.tecto.2013.11.024>
- Wang, K., & Hu, Y. (2006). Accretionary prisms in subduction earthquake cycles: The theory of dynamic Coulomb wedge. *Journal of Geophysical Research*, 111(6), 1–16. <https://doi.org/10.1029/2005JB004094>
- Wang, K., Hu, Y., Von Huene, R., & Kukowski, N. (2010). Interplate earthquakes as a driver of shallow subduction erosion. *Geology*, 38(5), 431–434. <https://doi.org/10.1130/G30597.1>
- Wessel, P., & Smith, W. H. F. (1991). Free software helps map and display data. *Eos, Transactions American Geophysical Union*, 72(41), 441. <https://doi.org/10.1029/90EO00319>
- Wessel, P., Smith, W. H. F., Scharroo, R., Luis, J., & Wobbe, F. (2013). Generic mapping tools: Improved version released [software]. *EOS Transactions AGU*, 94(45), 409–410. <https://doi.org/10.1002/2013EO450001>
- Xia, Y., Geersen, J., Klaeschen, D., Ma, B., Lange, D., Riedel, M., et al. (2021). Marine forearc structure of eastern Java and its role in the 1994 Java tsunami earthquake. *Solid Earth*, 12(11), 2467–2477. <https://doi.org/10.5194/se-12-2467-2021>
- Xia, Y., Klaeschen, D., Kopp, H., & Schnabel, M. (2022). Reflection tomography by depth warping: A case study across the Java trench. *Solid Earth*, 13(2), 367–392. <https://doi.org/10.5194/se-13-367-2022>
- Xia, Y., Kopp, H., Klaeschen, D., Geersen, J., Ma, B., & Schnabel, M. (2022a). Kirchhoff pre-stack depth migration images of the multi-channel seismic data, SO190, RV. SONNE [dataset]. Zenodo. <https://doi.org/10.5281/zenodo.7417572>
- Xia, Y., Kopp, H., Klaeschen, D., Geersen, J., Ma, B., & Schnabel, M. (2022b). Multi-beam bathymetry data offshore eastern Java margin [Dataset]. Zenodo. <https://doi.org/10.5281/zenodo.7417701>
- Yang, H., Liu, Y., & Lin, J. (2013). Geometrical effects of a subducted seamount on stopping megathrust ruptures. *Geophysical Research Letters*, 40(10), 2011–2016. <https://doi.org/10.1002/grl.50509>

Erratum

In the originally published version of this article, Figure 10 contained too many transparent vector units and nodes, resulting in corruption of the display of the figure. The figure has been replaced, and this version may be considered the authoritative version of record.